Direct observation and control of near-field radiative energy transfer in a natural hyperbolic material

L Abou-Hamdan, A Schmitt, R Bretel, S Rossetti, M Tharrault, D Mele, A Pierret, M Rosticher, T Taniguchi, K Watanabe, et al.

Direct observation and control of near-field radiative energy transfer in a natural hyperbolic material

L. Abou-Hamdan,[1,2,*] A. Schmitt,[3,*] R. Bretel,[3] S. Rossetti,[1,2] M. Tharrault,[3] D. Mele,[3,4] A. Pierret,[3] M. Rosticher,[3] T. Taniguchi,[5] K. Watanabe,[5] C. Maestre,[6] C. Journet,[6] B. Toury,[6] V. Garnier,[7] P. Steyer,[7] J. H. Edgar,[8] E. Janzen,[8] J-M. Berroir,[3] G. Fève,[3] G. Ménard,[3] B. Plaçais,[3] C. Voisin,[3] J-P. Hugonin,[9] E. Bailly,[9] B. Vest,[9] J-J. Greffet,[9] P. Bouchon,[2] Y. De Wilde,[1] and E. Baudin[3]

[1] *Institut Langevin, ESPCI Paris, PSL University, CNRS, 1 rue Jussieu, F-75005 Paris, France*
[2] *DOTA, ONERA, Université Paris-Saclay, F-91123 Palaiseau, France*
[3] *Laboratoire de Physique de l'Ecole Normale Supérieure, ENS, Université PSL, CNRS, Sorbonne Université, Université Paris-Cité, 24 rue Lhomond, 75005 Paris, France*
[4] *Univ. Lille, CNRS, Centrale Lille, Univ. Polytechnique Hauts-de-France, Junia-ISEN, UMR 8520-IEMN, F-59000 Lille, France.*
[5] *Advanced Materials Laboratory, National Institute for Materials Science, Tsukuba, Ibaraki 305-0047, Japan*
[6] *Laboratoire des Multimatériaux et Interfaces, UMR CNRS 5615, Univ Lyon, Université Claude Bernard Lyon 1, F-69622 Villeurbanne, France*
[7] *Université de Lyon, MATEIS, UMR CNRS 5510, INSA-Lyon, F-69621 Villeurbanne cedex, France*
[8] *Tim Taylor Department of Chemical Engineering, Kansas State University, Durland Hall, Manhattan, KS 66506-5102, USA*
[9] *Laboratoire Charles Fabry, IOGS, Université Paris-Saclay, F-91123 Palaiseau, France*

Heat control is a key issue in nano-electronics, where new efficient energy transfer mechanisms are highly sought after. In this respect, there is indirect evidence that high-mobility hexagonal boron nitride (hBN)-encapsulated graphene exhibits hyperbolic out-of-plane radiative energy transfer when driven out-of-equilibrium. Here we directly observe radiative energy transfer due to the hyperbolic phonon-polaritons modes of the hBN encapsulant in intrinsic graphene devices under large bias, using mid-infrared spectroscopy and pyrometry. By using different hBN crystals of varied crystalline quality, we engineer the energy transfer efficiency, a key asset for compact thermal management of electronic circuits.

I Introduction

Radiative energy transfer can be enhanced via the Purcell effect[1], which relies on the shaping of the local electromagnetic density of states (LDOS). This can be done by engineering the geometrical and dielectric properties of the structure. For instance, materials with a negative dielectric permittivity possess a large number of polaritonic near-field modes, which substantially augments the LDOS near the surface[2]. In this case, energy transfer is in general restricted to nanometric distances due to the limited range of surface polaritons[3–5].

Hyperbolic metamaterials have been proposed as a route for long-range radiative energy transfer as they host nonevanescent modes with large wavectors contributing to the large LDOS[6,7]. More recently, naturally hyperbolic materials have facilitated this approach[8,9]. In particular, the van der Waals material hexagonal Boron Nitride (hBN) possesses exceptionally well-defined hyperbolic phonon-polariton (HPhP) modes[10,11]. Consequently, the radiative thermal transfer induced by a hot source exceeds the vacuum far-field Planckian limit in graphene/hBN heterostructures[12–14]. However, probing from the source perspective the radiative energy transfer efficiency is challenging in such structure, owing to the parasitic contribution from thermal conduction.

Graphene/hBN heterostructures are the ideal platform for studying hyperbolic radiative energy transfer[15,16]: graphene is the quintessential candidate for nano-electronics[17] owing to its phonon-limited mobility at room temperature greatly surpassing that of silicon electronics. In diffusive graphene energy relaxation is mainly driven by electron-phonon-impurity super-collisions[18,19]. This energy transfer pathway is silenced in high-mobility graphene devices under large electrical bias due to their characteristically weak electron-intrinsic phonon coupling[20], so that radiative energy transfer is predominant[12,14,21]. As hBN-encapsulated graphene has no vacuum gap, the coupling between graphene's electrons and hBN's HPhPs is maximal, owing to the atomically flat surfaces of the two materials.

Under continuous electrical driving, graphene's electrons reach a strongly out-of-equilibrium electronic distribution[15,22] as interband Zener-Klein tunneling[15,23] injects electron-hole pairs in the graphene channel. This effect produces electroluminescence in the mid-infrared[24]. In this case, the driving mechanism of the emission is the non-thermal electronic distribution rather than the source-reservoir temperature difference as in usual thermal

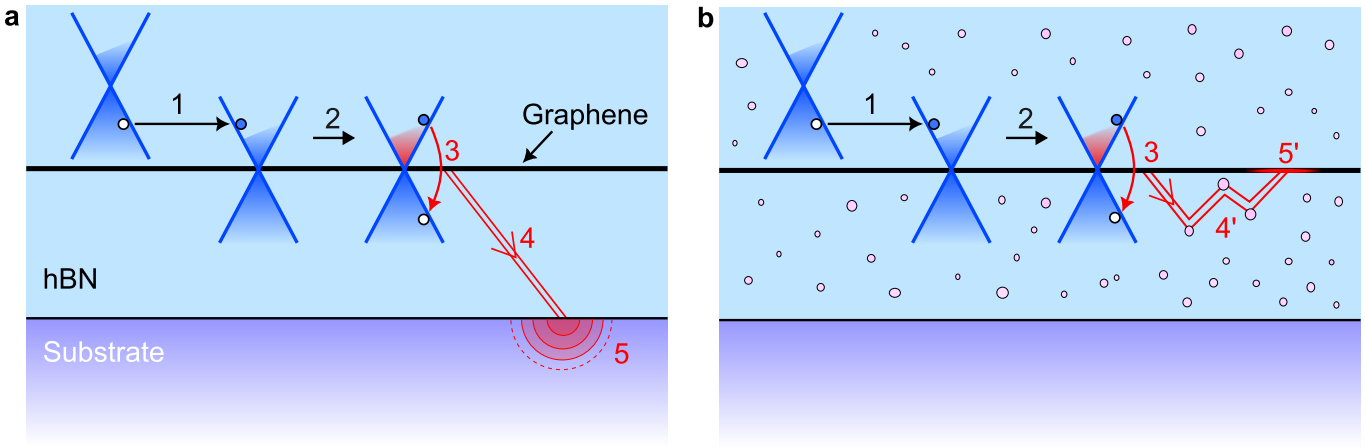

Fig 1: **Electroluminescent radiative energy transfer of graphene in pristine and turbid hBN encapsulate. a**, Energy transfer from graphene to the substrate (SiO_2 or Au) follows a 4-step process. (Step 1) Electrical Zener-Klein interband pumping under large applied bias. (Step 2) Intraband thermalization. (Step 3) Interband emission of a hyperbolic phonon-polariton (HPhP) of hBN. (Step 4) Ballistic HPhP propagation eventually reaches the substrate. (Step 5) HPhP energy transfer to the substrate results in a local temperature increase. **b**, In the case of turbid hBN, steps 1, 2, and, 3 are identical, but HPhPs are localized near the graphene layer due to scattering sites in the crystal (represented by pink bubbles) at step 4, leading to their re-absorption by the graphene electron gas at step 5. Consequently, in this case, the substrate remains cold.

transfer. Consequently, it exceeds Planckian hyperbolic radiative heat transfer[16]. The energy transfer process in the graphene/hBN heterostructure considered here, along with its electroluminescent emission of HPhP modes, is depicted in Fig. 1. The efficiency of the radiative energy transfer is then dictated by the ballisticity of the hyperbolic phonon-polaritons, as illustrated by Figure 1a and b. Utilising this ballisticity as a controlled parameter enables the engineering of radiative energy transfer.

In this study, we present a direct observation of hyperbolic radiative energy transfer by investigating hBN-encapsulated graphene devices in ambient conditions under very large bias. We use mid-infrared (mid-IR) spectroscopy[25–27] to reveal the spectral signatures of the HPhP energy carriers, and we monitor the out-of-plane power to the device's SiO_2 substrate, unambiguously demonstrating radiative energy transfer mediated by HPhPs. In addition, we show that the out-of-plane energy transfer efficiency can be controlled by tuning the crystalline quality of the hBN encapsulant. We find that ballistic HPhP propagation leads to substantial radiative energy transfer through pristine hBN (Fig. 1a), while HPhPs in turbid hBN are localized close to the graphene layer and thus re-absorbed (Fig. 1b).

II Hyperbolic phonon-polariton fingerprint in the far-field

We begin by experimentally revealing the HPhP modes that are actively involved in the energy transfer in a graphene device under large bias. Although these modes are confined to the near-field of the hBN layers, they can be measured in the far-field if sufficient local scatterers are present, leading to a measurable scattered signal in the far-field. For example, in the TR1 device (Fig. 2a, inset), significant scattering of the HPhPs occurs at the edge contact metallizations and the edges of the heterostructure (marked by red arrowheads). The measured mid-IR emission spectrum of TR1 under large bias is given in Fig. 2a along with that of a device in which scatterers are absent (hereafter referred to as TR2). While the latter only presents spectral features of the SiO_2 substrate, the spectrum of TR1 is dominated by a peak inside hBN's second *Reststrahlen* band ($\hbar\omega_{II} = 168.7 - 198.4$ meV, orange-shaded region in Fig. 2) at an energy of ~ 190 meV, with other peaks of lower amplitude within the *Reststrahlen* band. These peaks correspond to multiple HPhP branches resulting from the multiple orders of Fabry-Pérot resonances in the hBN thin film cavity, that have been previously revealed via scattering-scanning near-field optical microscopy (s-SNOM) measurements[10,11,28]. This observation is further confirmed by the calculation of the imaginary part of the reflection coefficient of the heterostructure in Fig. 2b, whose maxima indicate the HPhP mode branches. By looking at the spectral behaviour within SiO_2's *Reststrahlen* band (green-shaded region), we observe a resonance at SiO_2's surface phonon-polariton energy, indicated by a peak in the spectral flux at around 145 meV, which also appears in the corresponding calculations (see the weak local maximum of $\mathrm{Im}(r_p)$ in SiO_2's *Reststrahlen* band in panel b). This confirms the role of scatterers in

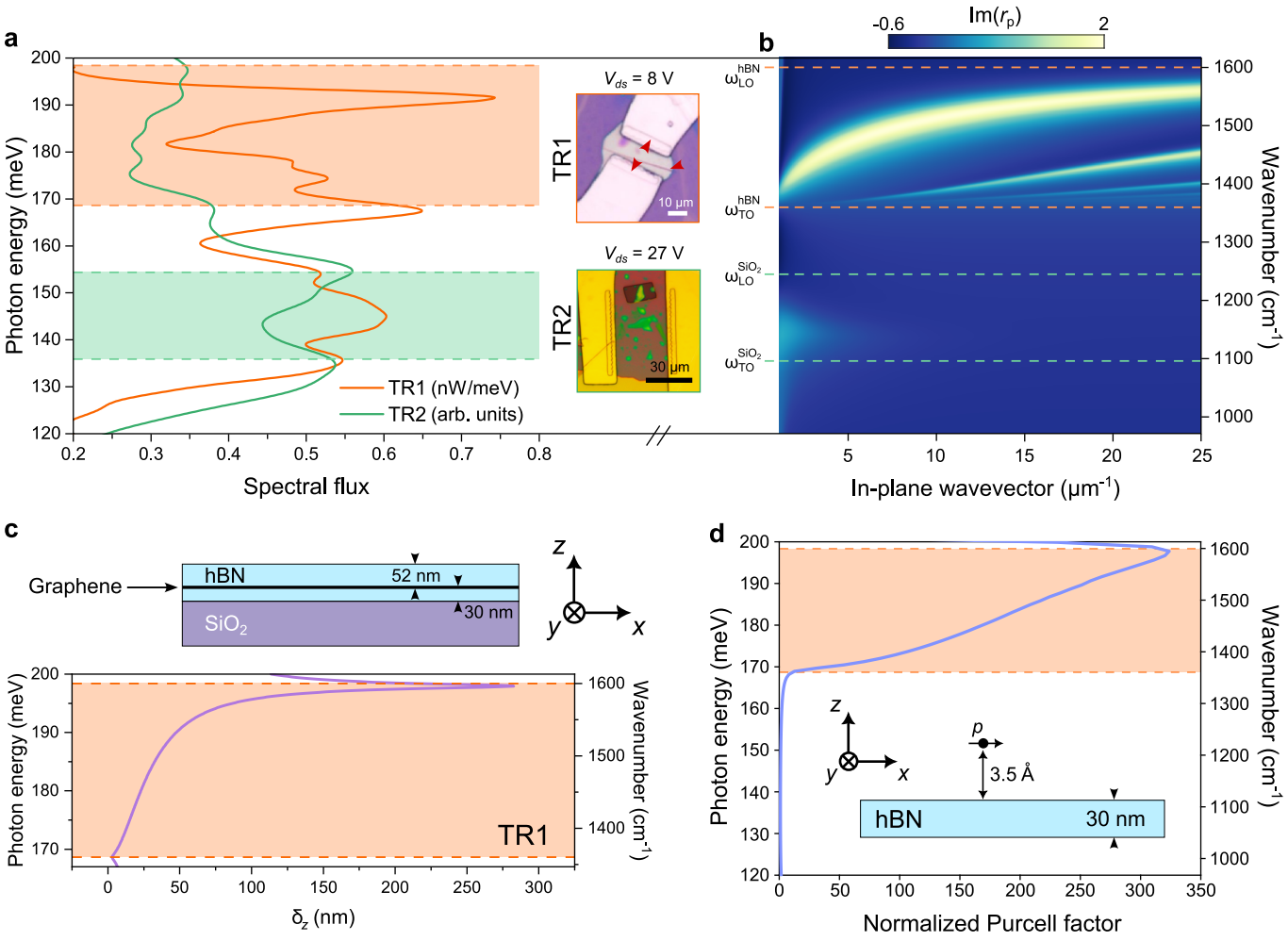

Fig 2: **Radiative origin of the out-of-plane energy transfer: scattering of HPhPs by defects. a**, Mid-infrared (mid-IR) spectrum of an electrically-biased hBN-encapsulated graphene device (TR1, inset). The small dimensions of this device's graphene channel ($9.2\,\mu$m $\times$ $15.5\,\mu$m) lead to increased scattering of the HPhP modes of the heterostructure by the edge contacts and etches in the hBN layer (marked by red arrowheads in the inset). The mid-IR spectrum of a larger graphene device (TR2, $35\,\mu$m $\times$ $35\,\mu$m, inset), in which scattering is absent, is shown for comparison. **b**, Imaginary part of the reflection coefficient (r_p) for p-polarized light incident upon the heterostructure consisting of TR1's polariton active layers (sketched in panel **c**). The polariton dispersion curves of the heterostructure can be visualized from the maxima of Im(r_p). See Supplementary information, section III for full details. The dashed green lines enclose the *Reststrahlen* band of SiO_2, while the dashed orange lines enclose hBN's second *Reststrahlen* band, in which $\mathrm{Re}(\varepsilon_x) = \mathrm{Re}(\varepsilon_y) < 0$ and $\mathrm{Re}(\varepsilon_z) > 0$, where $\varepsilon_{x,y}$ and ε_z are the in-plane and out-of-plane dielectric functions of hBN, respectively. **c**, Penetration depth δ_z of HPhPs in the z-direction (see main text) calculated for the layers of TR1 (top sketch). **d**, Purcell factor above a 30 nm-thick hBN cavity, given by $F_\mathrm{P} = \frac{3}{4\pi^2}\left(\frac{\lambda}{n}\right)^3 \frac{Q}{V}$, where λ is the free-space wavelength, n is the index of refraction of hBN, and Q and V are the quality factor and mode volume of the hBN cavity. F_P is computed for an in-plane dipole p situated 3.5 Å (*i.e.*, the inter-layer spacing in hBN) above the hBN layer and is normalized to its minimal value to elucidate its enhancement within hBN's *Reststrahlen* band (shaded region).

improving the sensitivity to near-field polariton modes. We verified that the mid-IR signal from the HPhP modes is unrelated to hBN's thermal emission by characterizing the device's blackbody radiation at various temperatures via an electrically controlled hot sample holder (see supplementary information for full details). hBN's polariton peak ($\sim$ 190 meV) appears in the measured thermal emission spectrum only for temperatures above ~ 200°C, while the hBN temperature under large bias, measured by Stokes anti-Stokes Raman thermometry (see Ref.[24]), is $\lesssim 75$°C.

Monitoring the HPhP mid-IR signal versus bias voltage shows that the onset of emission matches with the threshold of Zener-Klein tunneling extracted from DC transport measurements. Furthermore, we demonstrate in the supplementary information (section IV) the electroluminescent nature of the HPhP emission in the framework of the generalized Kirchhoff law[29], following a similar approach reported in Ref.[24].

We gain further insight regarding the ballistic HPhP-mediated energy transfer by examining the polariton

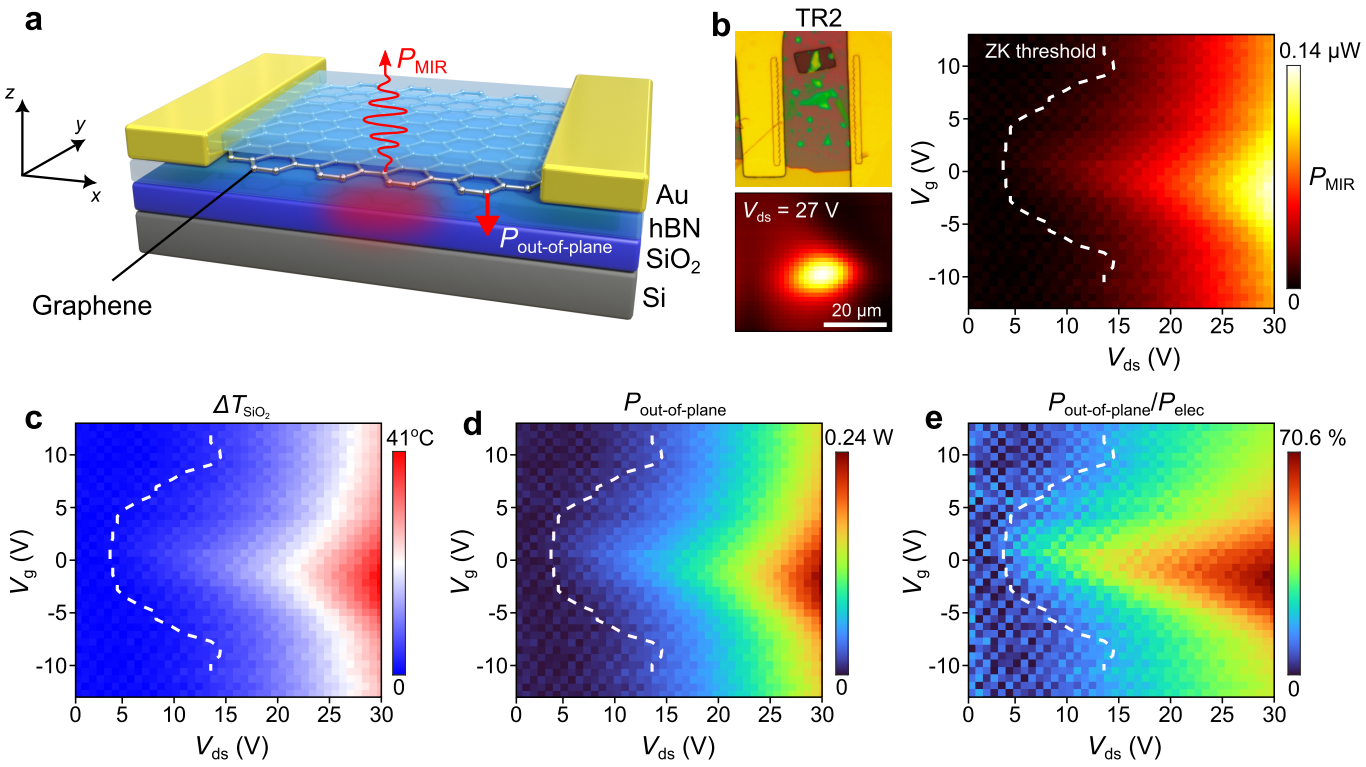

Fig 3: **Monitoring the out-of-plane energy transfer in a graphene device through its mid-infrared emission. a**, Schematic depiction of out-of-plane energy transfer in a high-mobility graphene field-effect device with an SiO_2 backgate. The back gate warms up slightly due to this out-of-plane energy transfer, emitting mid-infrared (mid-IR) thermal radiation. One can directly observe the device's out-of-plane energy transfer by monitoring the substrate's mid-IR emission. **b**, Left: microscope image (top) and spatial scan (bottom) of the spectrally integrated mid-IR signal (P_{MIR}, integrated over the detector's bandwidth, $\lambda = 6 - 14$ μm) emitted by the TR2 device under bias. The bright emission spot, between the source and drain electrodes, indicates that the signal is most intense in that region, revealing that the emission originates from beneath the device's channel. By contrast, the device's gold electrodes appear dark due to their low emissivity. Right: Scan of P_{MIR} as a function of electrical bias. The white dashed curve indicates the device's Zener-Klein (ZK) tunneling threshold. **c**, Measured temperature increase in the SiO_2 substrate as a function of bias. The temperature increase is determined by calibrating the detected mid-IR signal as a function of sample temperature (see SI for full details). **d**, Measured out-of-plane power $P_{\mathrm{out-of-plane}}$ as a function of applied bias. **e**, Ratio between $P_{\mathrm{out-of-plane}}$ and the total electrical power (P_{elec}) applied to the TR2 device.

penetration depth along the out-of-plane direction, which at the graphene/hBN interface is given by $\delta_z = |k_z|^{-1} = \left|\sqrt{\varepsilon_x\left(\frac{\omega^2}{c^2} - \frac{k_x^2}{\varepsilon_z}\right)}\right|^{-1}$, where ε_x and ε_z are the in-plane and out-of-plane dielectric functions of hBN, ω is the angular frequency, and k_x and k_z are the in-plane and out-of-plane polariton wavevectors. As shown in Fig. 2c, the polariton penetration depth near the transverse optical phonon energy of hBN ($\hbar\omega_{\mathrm{TO}}^{\mathrm{hBN}} \sim 169$ meV) is less than 25 nm, *i.e.*, shorter than the thickness of the bottom hBN layer (30 nm) separating the graphene layer and the SiO_2 back-gate in TR1. At higher energies, the penetration depth increases steadily, reaching a maximal value of 282 nm near the longitudinal optical phonon energy ($\hbar\omega_{\mathrm{LO}}^{\mathrm{hBN}} \sim 198$ meV). Concordantly, most of the energy is channeled through the lowest-order HPhP branch at this energy (see Fig. 2b). Note that this energy also corresponds to the largest Purcell factor, i.e. the largest LDOS enhancement (see Fig. 2d).

III Pyrographic signature of electroluminescent energy transfer

A direct indication of out-of-plane radiative energy transfer (Fig. 1a) in high-mobility graphene devices with an SiO_2/Si back-gate can be readily obtained by monitoring the device's far-field mid-IR emission as a function of electrical bias. At large bias, beyond the threshold for Zener-Klein tunneling, a fraction $P_{\mathrm{out-of-plane}}$ of the total electrical power injected into the device's channel is radiated towards the SiO_2 back-gate. This results in a slight warming of the

back-gate, which is subsequently signaled by the incandescent mid-IR emission of the SiO_2 substrate as depicted schematically in Fig. 3a. We first perform spectroscopy of the measured mid-IR signal of a large graphene device with an SiO_2/Si back-gate under large bias (TR2), which reveals signatures of the emission of the SiO_2 layer. Indeed, as shown in Fig. 2a (orange curve), the recorded spectrum possesses two peaks at the transverse and longitudinal optical phonon frequencies of SiO_2 ($\omega_{\mathrm{TO}}^{\mathrm{SiO_2}}$ and $\omega_{\mathrm{LO}}^{\mathrm{SiO_2}}$, respectively) and a dip in the middle of the *Reststrahlen* band (shaded region), that results from enhanced reflectance in this spectral region. We also verify through a spatial scan of the detected mid-IR signal (P_{MIR}), that the signal is most intense at the channel location (see Fig. 3b, bottom-left), indicating that the detected signal originates from the heated SiO_2 substrate beneath the channel. Note that in this spectral range, the mid-IR signal emitted from the graphene channel is negligible with respect to that of the substrate's incandescence.

Having established that the detected signal originates from the region beneath the device's graphene channel, we may now quantify the contribution of out-of-plane radiation to the device's total power budget. The total power balance is given by $P_{\mathrm{elec}} = P_{\mathrm{in-plane}} + P_{\mathrm{out-of-plane}}$, where $P_{\mathrm{elec}} = V_{ds} I_{ds}$ (V_{ds}, drain-source bias voltage; I_{ds}, drain-source current) is the electrical power and $P_{\mathrm{out-of-plane}}$ ($P_{\mathrm{in-plane}}$) is the power transferred in the out-of-plane (in-plane) direction. We calculate the device's equivalent thermal resistance, R_{th}, by solving the heat equation. This resistance is determined by dividing the average temperature increase of the SiO_2 layer beneath the channel by the out-of-plane power $P_{\mathrm{out-of-plane}}$ cast into it. (see SI, section III). The temperature increase $\Delta T_{\mathrm{SiO_2}}$ is determined by measuring the device's mid-IR signal (see Fig. 3b, right), where the temperature dependence of the mid-IR signal is calibrated by placing the device on a hot plate and measuring its thermal emission at various temperatures (see supplementary information section II for more details). As a result, we obtain the distribution of the temperature increase as a function of electrical bias, which is on the order of $\Delta T_{\mathrm{SiO_2}} \simeq 20 - 40$ °C beyond the Zener-Klein threshold (see Fig. 3c).

Following this model, $P_{\mathrm{out-of-plane}}$ and the ratio ($P_{\mathrm{out-of-plane}}/P_{\mathrm{elec}}$) of the out-of-plane transferred power to the total electrical power injected into the device can be computed as a function of electrical bias and doping, and the result is presented in Figs. 3d and e. The maps reveal that the investigated out-of-plane energy transfer mechanism plays a significant role in the device's total power budget, with a maximal contribution of about 71 %. We underscore here that this corresponds to an out-of-plane radiative power per surface area of ~ 19.5 kW/cm^2. This value is three orders of magnitude larger than the highest cooling power experimentally reported for a parent mechanism, namely the electroluminescent cooling in conventional semi-conductors[30–32]. Interestingly, the out-of-plane radiative power is highest at large bias near the charge-neutral point ($V_g = 0$) and falls off away from it due to Pauli blocking. Furthermore, the onset of out-of-plane energy transfer matches with the threshold of Zener-Klein tunneling extracted from DC transport measurements, as indicated by the dashed line in Fig. 3d. In fact, $P_{\mathrm{out-of-plane}}$ follows the same trend as that of the radiated power (P_{MIR}), whose onset is also given by the Zener-Klein tunneling threshold. In contrast, the electrical power shows the expected decrease near the charge-neutral point at large bias (see Fig. SI- 6a).

IV Engineering hyperbolic radiative energy transfer

Having demonstrated hyperbolic radiative energy transfer from graphene through hBN, we show how to engineer such energy transfer. To do so, we borrow a well-known concept from far-field optics in disordered media, which states that light in a highly turbid material can be back-scattered toward the source[33]. Far-field radiative energy transfer is therefore strongly reduced in such materials, in a manner that is analogous to the effect of clouds on the Earth's heat budget. This concept has been successfully used in the context of thermal conduction, where nanometer-scale acoustic defects were used as scatterers to control energy transfer[34]. Here we exploit this idea to control hyperbolic radiative energy transfer by tuning the density of scattering sites in hBN. Remarkably, hBN can be readily grown with such scattering sites while maintaining its extraordinary properties as a graphene encapsulant.

We demonstrate this property by considering two different sources of the hBN crystals used in our devices: in addition to the hBN fabricated under high pressure and high temperature[35] (denoted by HPHT-hBN in the following), we fabricated devices with hBN crystals prepared at lower and isostatic pressure through a polymer-derived ceramics (PDC-hBN in the following) route[36]. While devices using either hBN crystals present similar transport properties[37], such as large electronic mobility $\mu > 8$ m^2/V.s in ambient conditions, the PDC route being a more recent synthesis method, the hBN produced contains more scattering sites. Indeed, as investigated by cathodoluminescence, crystal defects presumably involving carbon or oxygen interstitial atoms are present in such crystals[38] so that radiative energy transfer is expected to be less efficient (see Fig. 1b). This is confirmed by a near-IR determination of graphene's electron temperature (see Fig. 4a), in which the electronic temperature is noticeably higher in the PDC-hBN device (reaching temperatures of $T \sim 900$ K at a maximal field of 0.7 V/μm, while we consistently measure $T \sim 600$ K on all devices made with HPHT-hBN). This behaviour is also corroborated by 1-10 GHz noise thermometry measurements (see SI), in which we compare the noise temperature of a device made with PDC-hBN and another made with HPHT-hBN.

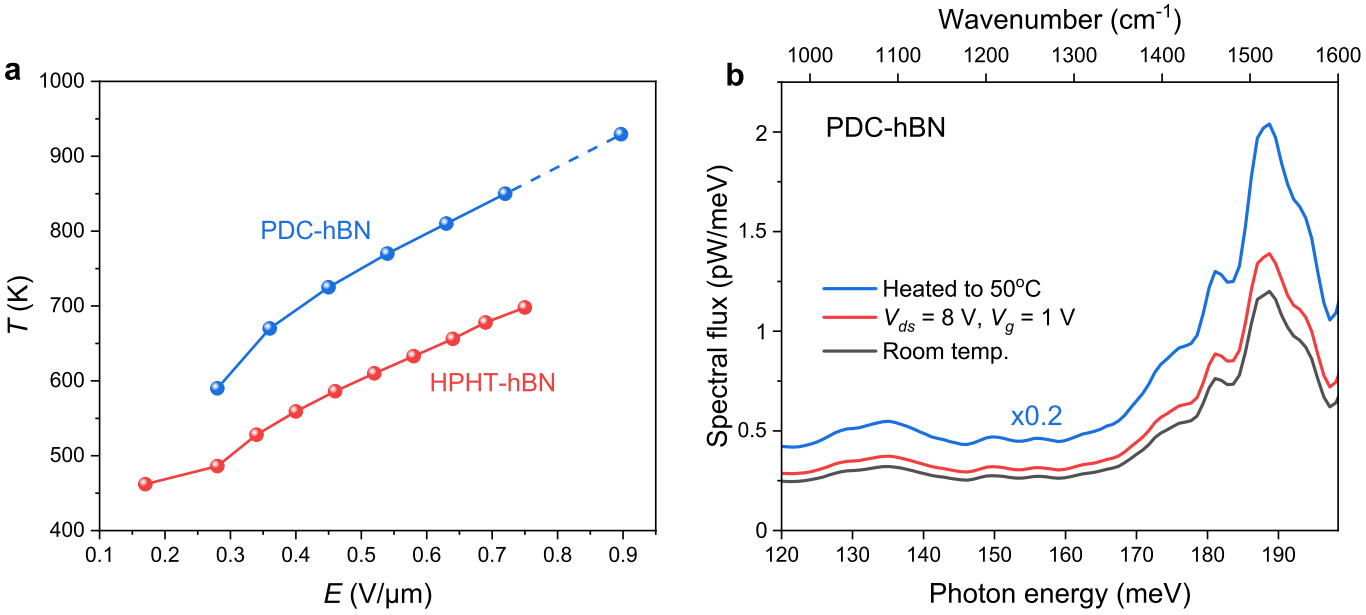

Fig 4: **Engineering energy transfer efficiency by tuning hBN crystalline quality.** **a**, Near-IR graphene electron temperature versus bias for the two devices Lyon1 (PDC-hBN) and F161 (HPHT-hBN), measured around a wavelength $\lambda = 1.5$ μm, for a doping $n = 6 \times 10^{11}$ cm^{-2}. **b**, Mid-IR characterization of a device made with PDC-hBN on a Si/SiO_2 back gate. Vertical energy transfer under large bias is monitored through the incandescence of the SiO_2 substrate, with a much weaker temperature increase $\Delta T_{SiO_2} \lesssim 1°C$, which corresponds to an out-of-plane radiative power per surface area of ~ 0.47 kW/cm^2., *i.e.*, only 2.4 % of that of devices made with HPHT-hBN.

Such HPhP-opaque materials open the door to new regimes with extremely out-of-equilibrium electronic distribution.

To further verify the suppression of HPhP energy transfer with PDC-hBN we conducted a similar study as the one reported in Section III, that is, we performed mid-IR spectroscopy on a PDC-hBN device on an SiO_2/Si back-gate and monitored the out-of-plane energy transfer through the incandescence of SiO_2. As shown in Fig. 4b, the temperature increase ΔT_{SiO_2} is $\lesssim 1°C$ at large bias, which is substantially smaller than the increase $\Delta T_{SiO_2} \simeq 20 - 40$ °C reported for the HPHT-hBN device TR1, resulting in a reduction in out-of-plane energy transfer down to only 0.47 kW/cm^2. Interestingly, far-field measurements performed on both hBN crystals revealed similar far-field optical properties, which suggests that scattering sites in PDC-hBN are present on a subwavelength scale.

Conversely, using isotopically pure[39] hBN with boron-11 and nitrogen-14, in which there is no mass disorder and phonon-polariton propagation length is doubled[40], leads to increased radiative energy transfer. This aligns with prior research on the faster cooling dynamics of graphene and larger interfacial conductance[41]. We verified by means of noise thermometry (see SI) that high-mobility graphene devices fabricated with boron-isotopically pure hBN present enhanced radiative energy transfer under large bias, validating our ability to tune HPhP energy transfer by engineering the hBN crystal.

V Conclusion

In summary, we have directly observed near-field radiative energy transfer mediated by the HPhP modes of hBN in hBN-encapsulated graphene devices under large bias. The mechanism for this energy transfer was shown to be electroluminescence from these HPhP modes, whose signature was observed in the far-field as a result of scattering by defects. The onset of such energy transfer was concomitant with the Zener threshold for interband carrier injection. We also determined the fraction of power channeled through this radiative transfer mechanism by monitoring the temperature increase of the underlying SiO_2 substrate via pyrometry. Radiative energy transfer was the dominant energy transfer mechanism accounting for ~ 71 % of the device's total power budget. We then demonstrated the engineering of the radiative energy transfer by tuning the turbidity of the hyperbolic hBN encapsulant, and as such the ballisticity of HPhPs. This was confirmed by comparing several hBN sources using multiple probes including mid-IR pyrometry, electronic noise and near-IR thermometries.

While it is well known that far-field radiative energy transfer is affected by the turbidity of the propagating

medium[33], our experimental study demonstrates for the first time that the concepts of optics in disordered media can be applied to the transport of radiative energy by near-field modes. This is possible because the hyperbolic phonon-polaritons involved in radiative energy transfer are extremely subwavelength electromagnetic *propagating* modes. In addition, controlling energy transfer by engineering a material's turbidity is appealing from a technological point of view: for example, it has been shown that the acoustic turbidity of a material makes it possible to control its thermal conduction without altering its macroscopic properties[34,42]. In our experiments, we have shown that, while radiative energy transfer is effectively suppressed when introducing defects in hexagonal Boron Nitride, its performance as an electronic encapsulant remains exceptional, thus validating this concept. This observation bodes well for applications in nanothermy and microelectronics.

VI Authors contributions

LAH, AS, BP, YDW and EmB conceived the experiments. AS conducted device fabrication and electrical measurements under the guidance of DM, AP and MR in the early developments. TT, KW, CM, CJ, VG, JHE and EJ provided the hBN crystals. LAH and SR made the MIR emission measurements with the help of AS and RB. AS performed the Raman thermometry measurements. MT performed the NIR measurements. LAH, AS, JJG, ElB, BV, YDW, CV, BP, JMB, GF, PB, GM and EmB analyzed the data and developed the theoretical interpretation. JPH wrote the numerical codes. LAH, AS, RB, YDW, and EmB wrote the manuscript with contributions from the co-authors.

VII Acknowledgments

The research leading to these results has received partial funding from the European Union Horizon 2020 research and innovation program under grant agreement No.881603 "Graphene Core 3", and from the French ANR-21-CE24-0025-01 "ELuSeM". This work has received support under the program “Investissements d’Avenir” launched by the French Government. JHE and EJ appreciate support for monoisotopic hBN crystal growth from the U. S. Office of Naval Research under award number N00014-22-1-2582.

VIII Additional information

Competing financial interests: The authors declare no competing financial interests.

IX Data availability

Data will be publicly available on Zenodo.

---

* These two authors contributed equally to this work.

[1] EM Purcell. Spontaneous emission probabilities at radio frequencies. In *Confined Electrons and Photons: New Physics and Applications*, pages 839–839. Springer, 1995.

[2] S Shen, A Narayanaswamy, and G Chen. Surface phonon polaritons mediated energy transfer between nanoscale gaps. *Nano Lett.*, 9(8):2909–2913, 2009.

[3] K Kim, B Song, V Fernández-Hurtado, W Lee, W Jeong, L Cui, D Thompson, J Feist, MT Homer Reid, FJ García-Vidal, JC Cuevas, E Meyhofer, and P Reddy. Radiative heat transfer in the extreme near field. *Nature*, 528:387–391, 2015.

[4] R St-Gelais, L Zhu, S Fan, and M Lipson. Near-field radiative heat transfer between parallel structures in the deep subwavelength regime. *Nat. Nanotechnol.*, 11:515–519, 2016.

[5] J DeSutter, L Tang, and M Francoeur. A near-field radiative heat transfer device. *Nat. Nanotechol.*, 14:751–755, 2019.

[6] R Messina, P Ben-Abdallah, B Guizal, M Antezza, and SA Biehs. Hyperbolic waveguide for long-distance transport of near-field heat flux. *Phys. Rev. B*, 94:104301, 2016.

[7] J Shi, B Liu, P Li, LY Ng, and S Shen. Near-field energy extraction with hyperbolic metamaterials. *Nano Lett.*, 15:1217–1221, 2015.

[8] K Korzeb, M Gajc, and DA Pawlak. Compendium of natural hyperbolic materials. *Opt. Express*, 23:25406–25424, 2015.

[9] P Li, M Lewin, AV Kretinin, JD Caldwell, KS Novoselov, T Taniguchi, K Watanabe, F Gaussmann, and T Taubner. Hyperbolic phonon-polaritons in boron nitride for near-field optical imaging and focusing. *Nature Communications*, 6:7507, 2015.

[10] S Dai, Z Fei, Q Ma, AS Rodin, M Wagner, AS McLeod, MK Liu, W Gannett, W Regan, K Watanabe, T Taniguchi, M Thiemens, G Dominguez, AH Castro Neto, A Zettl, F Keilmann, P Jarillo-Herrero, MM Fogler, and DN Basov. Tunable phonon polaritons in atomically thin van der Waals crystals of Boron Nitride. *Science*, 343:1125–1129, 2014.

[11] S Dai, Q Ma, MK Liu, T Andersen, Z Fei, MD Goldflam, M Wagner, K Watanabe, T Taniguchi, M Thiemens, F Keilmann, G C A M Janssen, SE Zhu, P Jarillo-Herrero, MM Fogler, , and DN Basov. Graphene on hexagonal boron nitride as a tunable hyperbolic metamaterial. *Nat. Nanotechnol.*, 10:682–686, 2015.

[12] A Principi, MB Lundeberg, NCH Hesp, KJ Tielrooij, F HL. Koppens, and M Polini. Super-Planckian electron cooling in a van der Waals stack. *Phys. Rev. Lett.*, 118:126804, 2017.

[13] KJ Tielrooij, N CH Hesp, A Principi, MB Lundeberg, EA A Pogna, L Banszerus, Z Mics, M Massicotte, P Schmidt, D Davydovskaya, D G Purdie, I Goykhman, G Soavi, A Lombardo, K Watanabe, T Taniguchi, M Bonn, D Turchinovich, C Stampfer, A C Ferrari, G Cerullo, M Polini, and F HL Koppens. Out-of-plane heat transfer in van der Waals stacks through electron–hyperbolic phonon coupling. *Nat. Nanotechnol.*, 13:41–46, 2018.

[14] EA A Pogna, X Jia, A Principi, A Block, L Banszerus, J Zhang, X Liu, T Sohier, S Forti, K Soundarapandian, B Terrés, JD Mehew, C Trovatello, C Coletti, F HL Koppens, M Bonn, HI Wang, N van Hulst, MJ Verstraete, H Peng, Z Liu, C Stampfer, G Cerullo, and KJ Tielrooij. Hot-carrier cooling in high-quality graphene is intrinsically limited by optical phonons. *ACS Nano*, 15:11285–11295, 2021.

[15] W Yang, S Berthou, X Lu, Q Wilmart, A Denis, M Rosticher, T Taniguchi, K Watanabe, G Fève, JM Berroir, G Zhang, C Voisin, E Baudin, and B Plaçais. A graphene Zener–Klein transistor cooled by a hyperbolic substrate. *Nat. Nanotechnol.*, 13:47–52, 2018.

[16] E Baudin, C Voisin, and B Plaçais. Hyperbolic phonon polariton electroluminescence as an electronic cooling pathway. *Adv. Funct. Mater.*, 30:1904783, 2020.

[17] KS Novoselov, VI Falko, L Colombo, PR Gellert, MG Schwab, and K Kim. A roadmap for graphene. *Nature*, 490:192–200, 2012.

[18] AC Betz, SH Jhang, E Pallecchi, R Ferreira, G Fève, JM Berroir, and B Plaçais. Supercollision cooling in undoped graphene. *Nat. Phys.*, 9:109–112, 2013.

[19] MW Graham, SF Shi, DC Ralph, J Park, and PL McEuen. Photocurrent measurements of supercollision cooling in graphene. *Nat. Phys.*, 9:103–108, 2013.

[20] AC Betz, F Vialla, D Brunel, C Voisin, M Picher, A Cavanna, A Madouri, G F'eve, JM Berroir, B Pla¸cais, and E Pallecchi. Hot electron cooling by acoustic phonons in graphene. *Phys. Rev. Lett.*, 109:056805, 2012.

[21] Qiang Liu, Wei Xu, Xiaoxi Li, Tongyao Zhang, Chengbing Qin, Fang Luo, Zhihong Zhu, Shiqiao Qin, Mengjian Zhu, and Kostya S Novoselov. Electrically-driven ultrafast out-of-equilibrium light emission from hot electrons in suspended graphene/hbn heterostructures. *International Journal of Extreme Manufacturing*, 6(1):015501, 2023.

[22] A Schmitt, P Vallet, D Mele, M Rosticher, T Taniguchi, K Watanabe, E Bocquillon, G Fève, JM Berroir, C Voisin, J Cayssol, MO Goerbig, J Troost, E Baudin, and B Plaçais. Mesoscopic Klein-Schwinger effect in graphene. *Nat. Phys.*, 19:830–835, 2023.

[23] N Vandecasteele, A Barreiro, M Lazzeri, A Bachtold, and F Mauri. Current-voltage characteristics of graphene devices: Interplay between Zener-Klein tunneling and defects. *Phys. Rev. B*, 82:045416, 2010.

[24] A Schmitt, L Abou-Hamdan, M Tharrault, S Rossetti, D Mele, R Bretel, A Pierret, M Rosticher, P Morfin, T Taniguchi, K Watanabe, JM Berroir, G Fève, G Ménard, B Plaçais, C Voisin, JP Hugonin, JJ Greffet, P Bouchon, Y De Wilde, and E Baudin. Electroluminescence of the graphene 2D semi-metal. *arXiv:2306.05351*, 2023.

[25] C Li, V Krachmalnicoff, P Bouchon, J Jaeck, N Bardou, R Haidar, and Y De Wilde. Near-field and far-field thermal emission of an individual patch nanoantenna. *Phys. Rev. Lett.*, 121:243901, 2018.

[26] L Abou-Hamdan, C Li, R Haidar, V Krachmalnicoff, P Bouchon, and Y De Wilde. Hybrid modes in a single thermally excited asymmetric dimer antenna. *Opt. Lett.*, 46(5):981–984, 2021.

[27] L Abou-Hamdan, L Coudrat, S Bidault, V Krachmalnicoff, R Haïdar, P Bouchon, and Y De Wilde. Transition from phononic to geometrical mie modes measured in single subwavelength polar dielectric spheres. *ACS Photonics*, 9(7):2295–2303, 2022.

[28] G Ni, AS McLeod, Z Sun, J R Matson, CF B Lo, DA Rhodes, FL Ruta, SL Moore, RA Vitalone, R Cusco, L Artus, L Xiong, CR Dean, JC Hone, AJ Millis, MM Fogler, JH Edgar, JD Caldwell, and DN Basov. Long-lived phonon polaritons in hyperbolic materials. *Nano Lett.*, 21:5767–5773, 2021.

[29] JJ Greffet, P Bouchon, G Brucoli, and F Marquier. Light emission by nonequilibrium bodies: Local Kirchhoff law. *Phys. Rev. X*, 8:021008, 2018.

[30] A Olsson, J Tiira, M Partanen, T Hakkarainen, E Koivusalo, A Tukiainen, M Guinea, and J Oksanen. Optical energy transfer and loss mechanisms in coupled intracavity light emitters. *IEEE Trans. Electron Devices*, 63:3567–3573, 2016.

[31] I Radevici, J Tiira, T Sadi, and J Oksanen. Influence of photo-generated carriers on current spreading in double diode structures for electroluminescent cooling. *Semicond. Sci. Technol.*, 33:05LT01, 2018.

[32] T Sadi, I Radevici, and J Oksanen. Thermophotonic cooling with light-emitting diodes. *Nat. Photon.*, 14:205–214, 2020.

[33] S Rotter and S Gigan. Light fields in complex media: Mesoscopic scattering meets wave control. *Rev. Mod. Phys.*, 89(1):015005, 2017.

[34] W Kim, J Zide, A Gossard, D Klenov, S Stemmer, A Shakouri, and A Majumdar. Thermal conductivity reduction and thermoelectric figure of merit increase by embedding nanoparticles in crystalline semiconductors. *Phys. Rev. Lett.*, 96:045901, 2006.

[35] T Taniguchi and K Watanabe. Synthesis of high-purity boron nitride single crystals under high pressure by using Ba–BN solvent. *J. Cryst. Growth*, 2:303, 2007.

[36] C Maestre, Y Li, V Garnier, P Steyer, S Roux, A Plaud, A Loiseau, J Barjon, L Ren, C Robert, B Han, X Marie, C Journet, , and B Toury. From the synthesis of hBN crystals to their use as nanosheets in van der Waals heterostructures. *2D Mater.*, 9:035008, 2022.

[37] A Schmitt, D Mele, M Rosticher, T Taniguchi, K Watanabe, C Maestre, C Journet, V Garnier, G F'eve, JM Berroir, C Voisin, B Pla¸cais, and E Baudin. High-field 1/f noise in hBN-encapsulated graphene transistors. *Phys. Rev. B*, 107:L161104, 2023.

[38] C Maestre, B Toury, P Steyer, V Garnier, and C Journet. Hexagonal boron nitride: A review on selfstanding crystals synthesis towards 2D nanosheets. *J. Phys.: Materials*, 4(4):044018, 2021.

[39] J Li, C Elias, G Ye, D Evans, S Liu, R He, G Cassabois, B Gil, P Valvin, B Liu, and JH Edgar. Single crystal growth of monoisotopic hexagonal boron nitride from a Fe–Cr flux. *J. Mater. Chem. C*, 8:9931–9935, 2020.

[40] AJ Giles, S Dai, I Vurgaftman, T Hoffman, S Liu, L Lindsay, CT Ellis, N Assefa, I Chatzakis, TL Reinecke, JG Tischler, MM Fogler, JH Edgar, DN Basov, and JD Caldwell. Ultralow-loss polaritons in isotopically pure boron nitride. *Nat. Mater.*, 17:134–139, 2018.

[41] A Brasington, S Liu, T Taniguchi, K Watanabe, JH Edgar, BJ LeRoy, and A Sandhu. Phonon lifetimes in boron-isotope-enriched graphene- hexagonal boron nitride devices. *Physica Status Solidi Rap. Res. Lett.*, 2200:030, 2022.

[42] B Poudel, Q Hao, Y Ma, Y Lan, A Minnich, B Yu, X Yan, D Wang, A Muto, D Vashaee, et al. High-thermoelectric performance of nanostructured bismuth antimony telluride bulk alloys. *Science*, 320(5876):634–638, 2008.

Supplementary information: Direct observation and control of near-field radiative energy transfer in a natural hyperbolic material

L. Abou-Hamdan,[1,2,*] A. Schmitt,[3,*] R. Bretel,[3] S. Rossetti,[1,2] M. Tharrault,[3] D. Mele,[3,4] A. Pierret,[3] M. Rosticher,[3] T. Taniguchi,[5] K. Watanabe,[5] C. Maestre,[6] C. Journet,[6] B. Toury,[6] V. Garnier,[7] P. Steyer,[7] J. H. Edgar,[8] E. Janzen,[8] J-M. Berroir,[3] G. Fève,[3] G. Ménard,[3] B. Plaçais,[3] C. Voisin,[3] J-P. Hugonin,[9] E. Bailly,[9] B. Vest,[9] J-J. Greffet,[9] P. Bouchon,[2] Y. De Wilde,[1] and E. Baudin[3]

[1] *Institut Langevin, ESPCI Paris, PSL University, CNRS, 1 rue Jussieu, F-75005 Paris, France*
[2] *DOTA, ONERA, Université Paris-Saclay, F-91123 Palaiseau, France*
[3] *Laboratoire de Physique de l'Ecole Normale Supérieure, ENS, Université PSL, CNRS, Sorbonne Université, Université Paris-Cité, 24 rue Lhomond, 75005 Paris, France*
[4] *Univ. Lille, CNRS, Centrale Lille, Univ. Polytechnique Hauts-de-France, Junia-ISEN, UMR 8520-IEMN, F-59000 Lille, France.*
[5] *Advanced Materials Laboratory, National Institute for Materials Science, Tsukuba, Ibaraki 305-0047, Japan*
[6] *Laboratoire des Multimatériaux et Interfaces, UMR CNRS 5615, Univ Lyon, Université Claude Bernard Lyon 1, F-69622 Villeurbanne, France*
[7] *Université de Lyon, MATEIS, UMR CNRS 5510, INSA-Lyon, F-69621 Villeurbanne cedex, France*
[8] *Tim Taylor Department of Chemical Engineering, Kansas State University, Durland Hall, Manhattan, KS 66506-5102, USA*
[9] *Laboratoire Charles Fabry, IOGS, Université Paris-Saclay, F-91123 Palaiseau, France*

I Sample fabrication and properties

The hexagonal-boron-nitride (hBN)-encapsulated graphene heterostructures are fabricated with the standard pick-up and stamping technique, using a polydimethylsiloxane(PDMS)/ polypropylene carbonate (PPC) stamp. When needed, the gate electrode is first fabricated on a high-resistivity Si substrate covered by a 285 nm-thick SiO_2 layer. It consists of a pre-patterned gold pad (80 nm thick) designed by laser lithography and Cr/Au metalization. The hBN/Graphene/hBN heterostructure is then deposited on top of the back-gate. This is followed by acetone cleaning of the stamp residues, Raman spatial mapping, and AFM characterization of the stack. Graphene edge contacts are then created by means of laser lithography and reactive ion etching, securing low contact resistance $\lesssim 1\ \mathrm{k\Omega}.\mu\mathrm{m}$. Finally, metallic contacts to the graphene channel are designed via a Cr/Au Joule evaporation. The transistors' dimensions are maximized to get the highest optical signal, while their high mobility $\mu \gtrsim 4\,\mathrm{m}^2.\mathrm{V}^{-1}.\mathrm{s}^{-1}$ at room temperature secures a moderate channel electric field $E = V/L \gtrsim 10^5\ \mathrm{V/m}$ for the threshold of electroluminescent near-field radiative energy transfer.
The properties of the different devices are summarized in Table I.

Device	**Length** (μm)	**Width** (μm)	μ ($\mathrm{m}^2/\mathrm{V.s}$)	**Contact resistance** (Ω)
TR1	9.2	15.5	6	250
TR2	35	35	10	150
PDC-hBN	9	9	4	230
HPHT-hBN	6	10	16	45
KSU-hBN	19	6	8	400

Table I: Geometrical and electronic properties of the different graphene transistors.

II Pyrography of an hBN-encapsulated graphene device with an SiO_2 back gate: mid-infrared experimental details

The mid-infrared (mid-IR) characterization techniques employed in this study have been outlined in detail elsewhere in Ref.[1]. We only illustrate here the calibration procedure used to determine the temperature increase of the device's

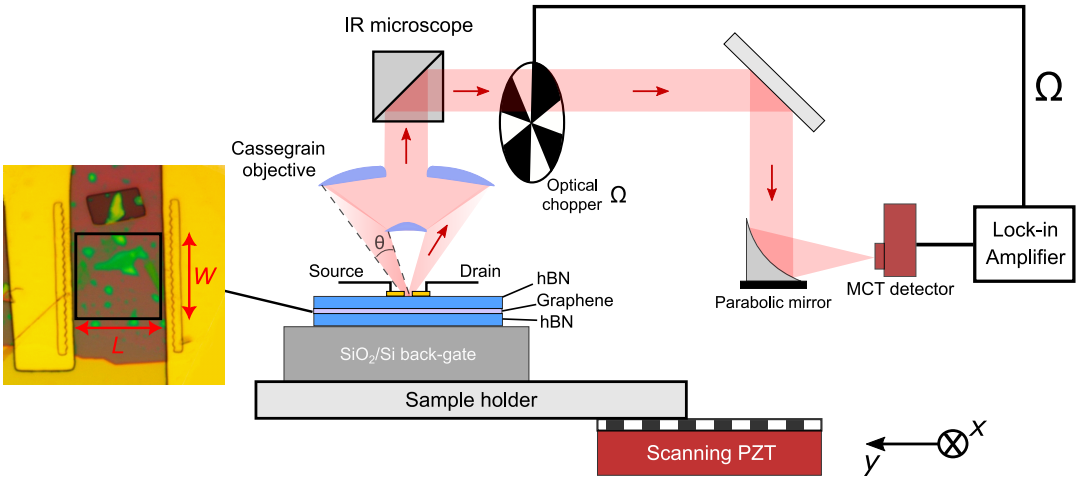

Fig. SI- 1: Schematic illustration of the detection technique used for characterizing the mid-IR signal (P_{MIR}, integrated over the full spectral range of the detector) of an hBN-encapsulated graphene device (left, $L \times W = 35 \times 35\ \mu\mathrm{m}^2$) due to the radiative emission of the SiO_2 back-gate.

SiO_2 back-gate due to near-field radiative energy transfer.

The far-field mid-IR emission of the device is collected via an IR microscope and optically chopped before reaching a liquid nitrogen-cooled MCT detector (see Fig. SI- 1). Spectroscopy or integrated signal mapping is then performed on the detected signal, as outlined in Ref.[1].

The out-of-plane radiative power of the device $P_{\mathrm{out-of-plane}}$ is determined from the device's detected mid-IR signal as a function of electrical bias (Fig. SI- 2**c**). This is done by calibrating the amplitude of the detected mid-IR signal with respect to the sample temperature by placing the sample on a hot sample holder and measuring its thermal emission at various temperatures (see Fig. SI- 2**a** and **b**). As a result of this calibration procedure, we find that the temperature increase of the SiO_2 substrate as a function of bias ranges between $\Delta T_{\mathrm{SiO_2}} \simeq 20 - 40°\mathrm{C}$ beyond the Zener-Klein threshold (Fig. SI- 2**d**).

Finally, we note here that the spectra reported in Figs. 2 and 4 of the main text were measured via infrared spatial modulation spectroscopy (IR-SMS)[2–4], as described in Ref.[1].

III Modeling the out-of-plane energy transfer in a graphene/hBN heterostructure

In this section, we detail various thermal models that describe energy transfer in a graphene/hBN device with an SiO_2/Si back-gate, starting from the simplest case (in which only the thermal resistance of the substrate is considered) then making our way through a more refined approach, in which the whole structure is modeled. The latter model is utilized to obtain the results presented in the main text.

The out-of-plane radiative power can be calculated via a simple thermal model (introduced in Ref.[5]) which only takes into account the thermal resistances of the SiO_2 and Si layers of the device's back-gate (see Fig. SI- 3). In this framework, the out-of-plane power is given by

$$\begin{aligned} P_{\mathrm{out-of-plane}} &= \frac{\Delta T_{\mathrm{SiO_2}}}{R_{\mathrm{th}}} \\ &= \frac{\Delta T_{\mathrm{SiO_2}}}{R_{\mathrm{SiO_2}} + R_{\mathrm{Si}}}, \end{aligned} \tag{1}$$

where R_{th} is the total effective thermal resistance of the layers and $R_{\mathrm{SiO_2}}$ and R_{Si} are the effective thermal resistances of the SiO_2 and Si layer, respectively (see Fig. SI- 3), which are given by

$$R_{\mathrm{SiO_2}} = \frac{t_{\mathrm{SiO_2}}}{2\kappa_{\mathrm{SiO_2}} LW}. \tag{2}$$

and,

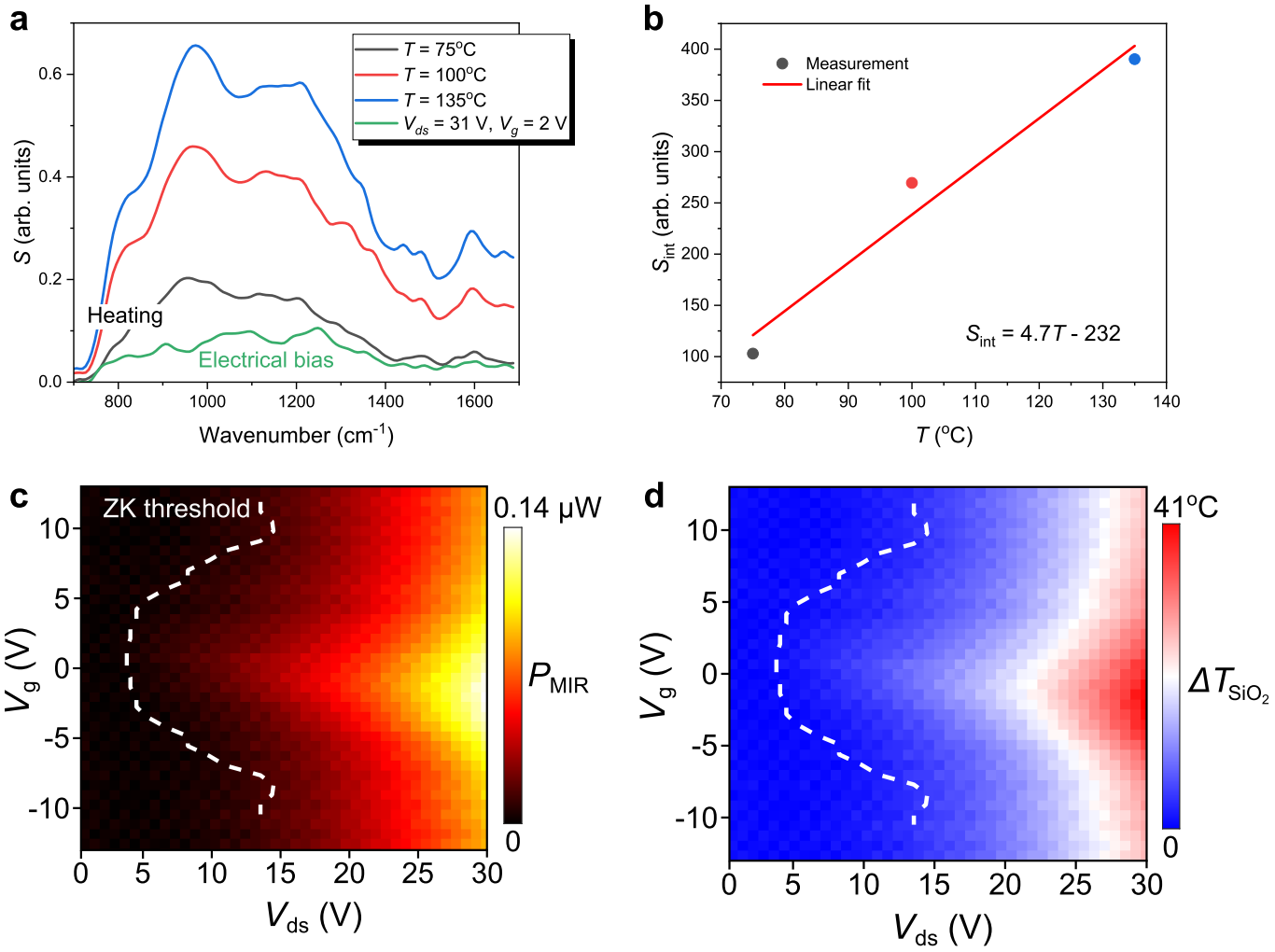

Fig. SI- 2: **a**, Comparison between the mid-IR spectra of the hBN-encapsulated device of panel **d** with an SiO_2 back gate under electrical bias and by heating the device via a hot plate at various temperatures T. The mid-IR signal is measured using an optical chopper (see Fig. SI- 1). The plotted spectra are corrected by a reference measurement, which removes the contribution of the chopper to the detected signal, and then normalized by an instrumental response function (see supplementary information of Ref.[1]). **b**, Linear fit of the spectrally-integrated signal S_{int} obtained with the hot plate as a function of temperature. S_{int} is found by integrating the spectra S from panel **a** over the detector's spectral bandwidth. From the comparison of panel **a** we find that the temperature of SiO_2 back-gate varies between $\Delta T_{\text{SiO}_2} \simeq 0 - 40$ °C when the device is electrically biased. **c**, Scan of the mid-IR spectrally-integrated power P_{MIR} emitted by the TR2 device as a function of bias. **d**, Increase in the temperature of the device's SiO_2 back-gate (ΔT_{SiO_2}) as a function of electrical bias, obtained from the mid-IR signal to sample temperature calibration.

$$R_{\text{Si}} = \frac{1}{2\kappa_{\text{Si}}\sqrt{LW}}, \tag{3}$$

In the above equations $t_{\text{SiO}_2} = 285$ nm is the thickness of the SiO_2 layer, $\kappa_{\text{SiO}_2} = 1.4$ W/m.K and $\kappa_{\text{Si}} = 150$ W/m.K are the thermal conductivities of SiO_2 and Si, and $L = 35$ μm and $W = 35$ μm give the dimensions of the device's graphene channel (see Fig. SI-3). From Eqs. (2) and (3), we obtain a total thermal resistance $R_{\text{th}} \simeq 178$ K/W. This results in an out-of-plane power $P_{\text{out-of-plane}}$ that reaches 68 % of the total electrical power injected into the device. Note that this simple model is the same as that reported in Ref.[5], however, in our case, there is an additional factor of 2 in the denominator of Eq. (2) to account for the fact that the thermal radiation emitted by the device results from the average temperature of the SiO_2 layer.

A more detailed approach for calculating $P_{\text{out-of-plane}}$ involves solving the general heat equation for a more complicated geometry. In its three-dimensional Cartesian form, the transient heat conduction equation is expressed as

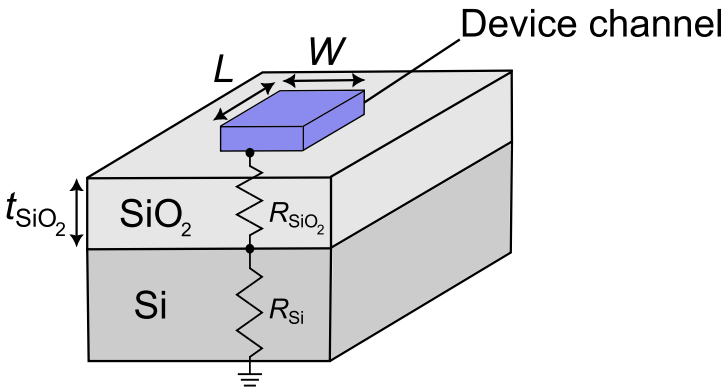

Fig. SI- 3: Sketch of a simple thermal model used to compute the total thermal resistance $R_{\rm th} = R_{\rm SiO_2} + R_{\rm Si}$ ruling the out-of-plane energy transfer in an hBN-encapsulated graphene device with a SiO_2/Si back-gate.

$$\rho C_p \frac{\partial T}{\partial t} = \nabla \cdot (\kappa \nabla T) + Q_{\rm th}, \tag{4}$$

where ρ represents the material density, C_p the specific heat capacity, T the temperature, t the time, κ the thermal conductivity, $\nabla\cdot$ the divergence and $Q_{\rm th}$ the heat generation term.

We consider in what follows a steady-state scenario with a cylindrical geometry (Fig. SI- 4), where the graphene transistor under large bias generates a disk-shaped heat flux (represented in red) on top of the SiO_2/Si substrate.

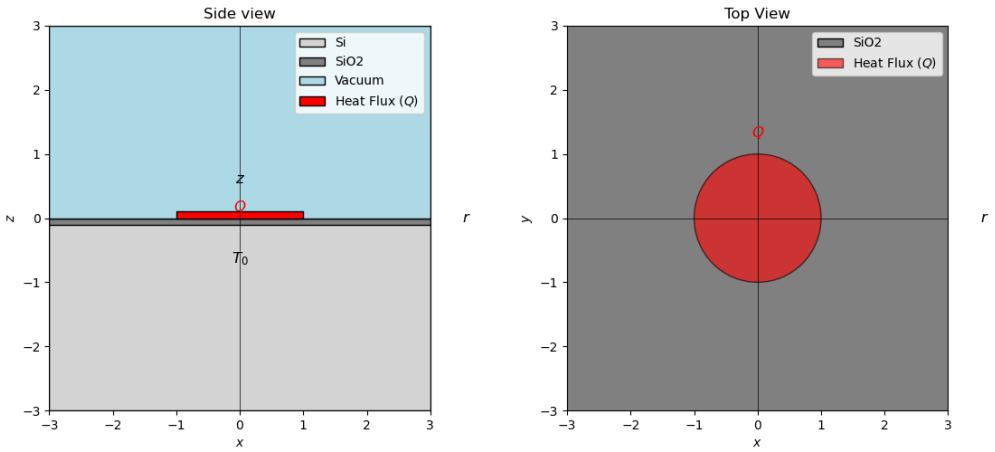

Fig. SI- 4: Side view (left panel) and top view (right panel) of the considered simple geometry, where a disk-shaped heat flux is applied on top of a 285 nm-thick SiO_2 layer and a semi-infinite Si substrate. Scales are in units of the disk radius R.

In this case the heat equation is given by

$$\frac{1}{r}\frac{\partial}{\partial r}\left(r\kappa_{rr}(r,z)\frac{\partial T}{\partial r}\right) + \frac{\partial}{\partial z}\left(\kappa_{zz}(r,z)\frac{\partial T}{\partial z}\right) = -Q_{\rm th}, \tag{5}$$

where $\kappa_{rr}(r,z)$ and $\kappa_{zz}(r,z)$ are the spatially dependent thermal conductivities (taking into account uniaxial materials such as hBN).

Table II summarizes the thermal conductivities of the different materials considered in the heat transfer problem.

We considered two different geometries:

Material	**Thermal conductivity** (W/m.K)
SiO_2	1.4
Si	150
hBN (in-plane)[6]	400
hBN (out-of-plane)[7]	8
Au	320

Table II: Thermal conductivities of the materials.

– The simple geometry considered in the model of Ref.[5], where a silicon dioxide layer extends from $z = 0$ to $z = -285$ nm on top of a semi-infinite (thickness 525 μm) Si substrate. A small disk-shaped heat flux is applied at the position of the graphene channel under bias (disk between $r = 0$ and $r = R$, with the radius of the disk $R = 19.7\,\mu$m chosen to mimic the total surface of the graphene transistor TR2 under study). Both layers extend from $r = 0$ to $r = 1$ mm and have distinct thermal properties. Such geometry is displayed in Fig. SI- 4.

– A more realistic geometry shown in Fig. SI- 5, where we add (i) an additional layer of hBN situated on top of the SiO_2 layer and located radially from $r = R$ to $r = 2R$ (hBN hollow disk) and vertically from $z = 0$ to $z = 80$ nm. This layer models the fraction of hBN outside of the graphene region that has been etched to create edge contacts. We also add (ii) gold metallizations, with an Au disk located atop the hBN hollow disk (thickness 150 nm) and an outer Au disk located everywhere outside the hBN region (from $r = 2R$ to $r = 1$ mm). These two disks represent the gold access that we deposit for the electrodes.

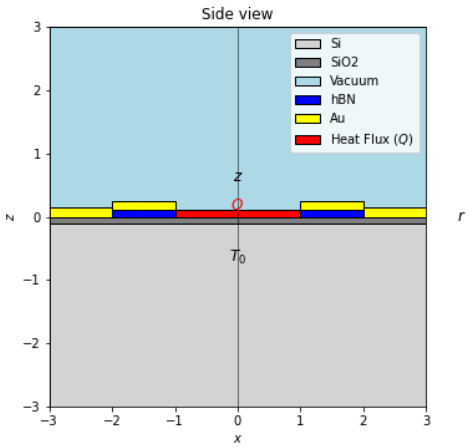

Fig. SI- 5: Side view of the considered more realistic geometry, where gold metallizations and a hollow hBN disk are present. Scales are in units of the disk radius R.

The aforementioned steady-state heat equation is solved numerically using the Finite-Element Method (FEM) in Mathematica. The solution domain is discretized into finite elements and the equation is solved over these elements. The boundary conditions define the fixed heat flux on top and the fixed temperature at the bottom of the structure. Finally, the spatial variation in the thermal conductivity is encoded by defining a piecewise function for k_r and k_z to account for these variations across different regions of the domain.
Table III compares the different scenarios and compares the obtained values for the thermal resistance with the value obtained with the simple model introduced in the main text, where we consider the average temperature for the SiO_2 layer. It underlines that the simple model outlined at the beginning of this section is in excellent agreement with a more refined treatment of the whole structure, and confirms that the out-of-plane radiative power reaches almost 70% of the total dissipated electrical power. Note that this result relies on three assumptions:

– SiO_2 layer is thin enough so that we consider it almost transparent, making the emission power additive with the SiO_2 layer depth

– Interference effects are negligible in the contribution from each layer depth to the far field

– The elevation in temperature is small compared to room temperature so that we can use the linearized version of the emitted power with respect to temperature elevation. We also assume an affine temperature profile within SiO_2 (which is confirmed by simulations).

Model	**Thermal resistance** (K/W)
Basic model[5]	178.33
Heat equation w/ SiO_2 and Si (Fig. SI- 4)	172.72
Addition of hBN hollow disk	171.9
Introduction of Au metallization (Fig. SI-5)	171.44

Table III: Thermal resistances obtained for the different models (for $R = 19.7$ μm mimicking the device TR2)

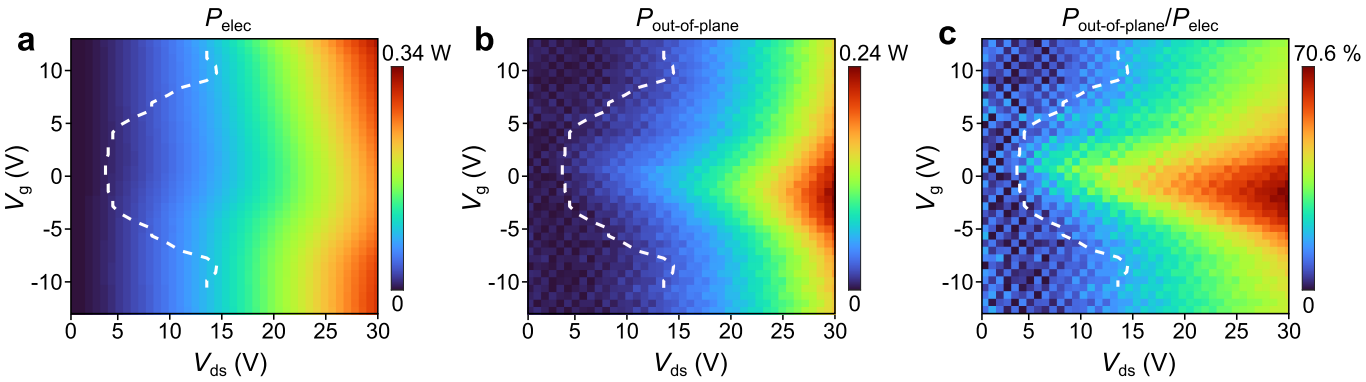

Fig. SI- 6: **a**, Total electrical power (P_{elec}) injected into the TR2 device as a function of bias. **b**, Out-of-plane dissipated power ($P_{\text{out}-\text{of}-\text{plane}}$) in the TR2 device as a function of electrical bias, computed from $P_{\text{out}} = \Delta T_{SiO_2}/R_{\text{th}}$, where $\Delta T_{SiO_2} \simeq 0 - 40$ °C and $R_{\text{th}} \simeq 171.4$ K.W^{-1} (see Table III and Fig. SI- 2**d**). **c**, Percentage giving the contribution of the out-of-plane radiative energy transfer mechanism to the total power budget obtained from the ratio $\frac{P_{\text{out}-\text{of}-\text{plane}}}{P_{\text{elec}}} = \frac{P_{\text{out}-\text{of}-\text{plane}}}{(P_{\text{out}-\text{of}-\text{plane}}+P_{\text{in}-\text{plane}})}$, where $P_{\text{in}-\text{plane}}$ is the in-plane power.

The out-of-plane power resulting from the solution of the full thermal problem is plotted in Fig. SI- 6**b** along with the ratio between $P_{\text{out}-\text{of}-\text{plane}}$ and the total electrical power P_{elec} injected into the device (Fig. SI- 6**c**), which gives the contribution of out-of-plane radiative near-field energy transfer to the device's total power budget (Fig. SI- 6**a**).

IV Electroluminescence origin of the measured mid-IR signal

We proceed to show in this section the electroluminescent nature of the mid-IR signal emitted by the devices under study here, following the approach adopted in Ref.[1]. Namely, we will experimentally rule out the possibility that the detected signal originates from the incandescence of hBN's optical phonons or from graphene's hot electrons. To do so, we measure the temperature of the two aforementioned quasi-particles, which is then used to estimate their blackbody emission. The temperature of hBN's optical phonons as determined via Raman Stokes-anti-Stokes thermometry is ~ 75°C (see Ref.[1] for full details). In Fig. SI-7, we compare the mid-IR spectrum of the TR1 device under electrical bias with that of its mid-IR thermal emission when the whole device is heated via a hot plate to the temperature of hBN's phonons (348 K). This comparison reveals that the main polariton peak at ~ 190 meV, which is involved in the out-of-plane energy transfer in the device under bias (see main text), is notably absent from the thermal emission spectrum (see Fig. SI-7, green curve). The polariton peak of the SiO_2 substrate (~ 145 meV) is likewise missing in the thermal emission spectrum. The main peak in the device's incandescence spectrum corresponds to a quarter-wave resonance of the heterostructure at around 170 meV (see Ref.[1]). Thus, incandescence from hBN's optical phonons can be dismissed as the origin of the mid-IR signal.

The temperature of graphene's hot electrons is measured by characterizing the device's near-infrared incandescence as outlined in Ref.[1]. The obtained electron temperatures are shown in Table IV as a function of bias. The mid-IR spectrum of the TR1 device is measured via IR-SMS as a function of increasing bias (Fig. SI-8**a**) and the resulting

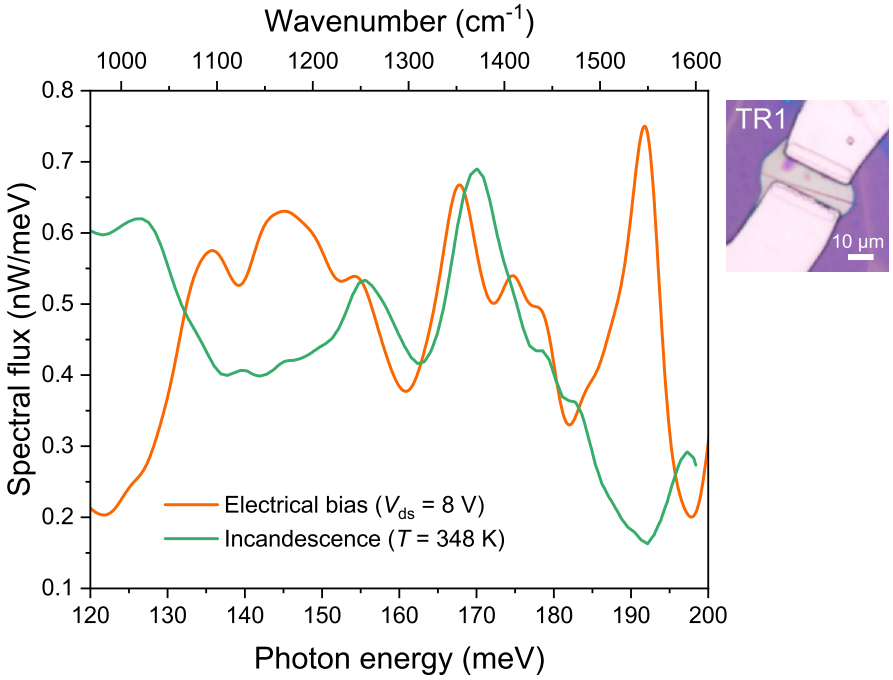

Fig. SI- 7: **Electroluminescence vs hBN incandescence.** Comparison between the IR-SMS spectral flux of TR1 under electrical bias (orange curve) and its incandescence when heated via a hot plate to the temperature of hBN's optical phonons (green curve).

$V_{ds}(V)$	T_e (K)
4.3	480
5.2	510
6.2	550
7.5	600
8.2	625

Table IV: Measured electron temperature (T_e) as a function drain-source voltage (V_{ds}).

spectral flux at the polariton peak, marked by a cross in Fig. SI-8**a**, is fitted with a Planck blackbody distribution using the electron temperatures listed in Table IV. This comparison shows that the measured spectral flux with increasing bias is about two times larger than that expected from incandescence in the bias range $6-8$ V (see Fig. SI-8**b**), thus precluding graphene's incandescence as a possible source of the measured signal. Note that this fitting procedure represents a worst-case scenario, in which it is assumed that the measured mid-IR flux at a low value of bias (4.3 V) is equal to that of the incandescence flux and the evolution of the two fluxes is compared as a function of increasing bias.

We conclude from the analysis above that the mid-IR signal emitted by the device under electrical bias is electroluminescent in nature.

V Hyperbolic phonon-polariton dispersion curves in hBN-encapsulated graphene

The polaritonic dispersion curves of our samples were obtained by evaluating the poles of the reflection coefficient r_p of the sample's multi-layer heterostructure for p-polarized light. A similar approach was utilized in Refs.[8,9].

Our samples consist of a mono-layer graphene encapsulated by two thin hBN flakes and placed on a SiO_2/Si substrate with a 285 nm-thick SiO_2 layer and an Si layer of bulk thickness. If we consider the SiO_2 thin film on the Si substrate only, then the surface phonon-polaritons supported by this layered system should exhibit two polariton branches ω_+ and ω_- with large wavevector asymptotic values of their dispersion curves reached when $\mathrm{Re}(\varepsilon_{SiO_2}) = -1$ for the upper polariton ω_+, and $\mathrm{Re}(\varepsilon_{SiO_2}) = -\varepsilon_{Si} = -11.7$ for the lower polariton branch ω_-[10,11], where ε_{SiO_2} and ε_{Si} are the dielectric functions of SiO_2 and Si, respectively. Nevertheless, the large damping inherent to amorphous SiO_2 precludes the excitation of the lower polariton branch, as the minimal value of the real part of ε_{SiO_2} is $\min\{\mathrm{Re}(\varepsilon_{SiO_2})\} \approx -2.43$

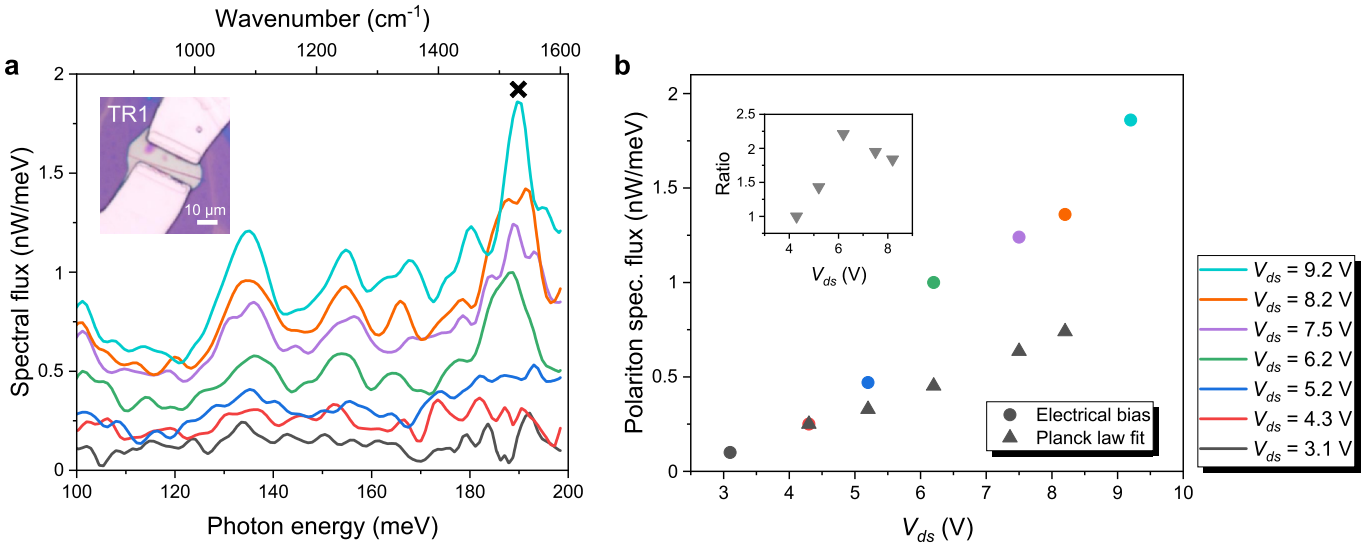

Fig. SI- 8: **Electroluminescence vs graphene's hot electron incandescence.** **a**, Sweep of the mid-infrared spectral emission of a graphene device TR1 (inset) under electrical bias, measured via IR-SMS. Legend keys to the right of panel **b**. **b**, Spectral flux at the polariton peak, marked by a cross in panel **a**, as a function of applied bias. The grey triangles are the Planck law fit given by $AE^3/[\exp(E/k_BT_e)-1]$, in which A is a fitting constant, $E = 190$ meV is the polariton energy, and T_e is the electron temperature given in Table IV. A is determined by equating the spectral flux at $V_{ds} = 4.3$ V to the value of the measured spectral flux at the same point. The inset shows the ratio of the measured spectral flux to that obtained from the Planck law fit.

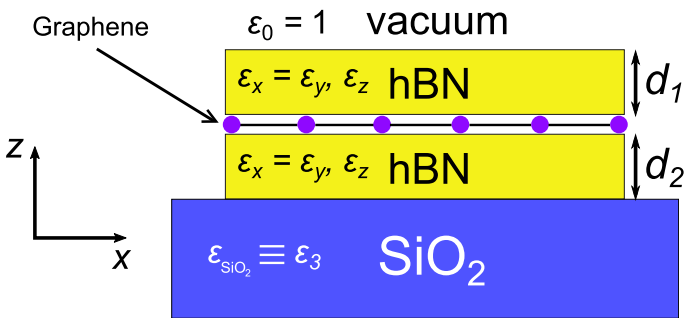

Fig. SI- 9: Sketch of a graphene layer encapsulated between two hBN thin films of thicknesses d_1 and d_2.

(see Fig. SI- 10 (c)). The polaritonic response, in this case, is independent of the SiO_2 layer thickness, *i.e.*, the response is the same as that of bulk SiO_2. Thus, to fully describe the polaritonic response of our samples, it is sufficient to consider a four-layered hBN/graphene/hBN/SiO_2 heterostructure, as sketched in Fig. SI- 9.

We use a *Drude-Lorentz* model with a single oscillator to describe the in-plane ($\varepsilon_x = \varepsilon_y$) and out-of-plane ($\varepsilon_z$) dielectric functions of hBN, as well as the dielectric function of SiO_2 (ε_{SiO_2}), that is

$$\varepsilon_\mu(\omega) = \varepsilon_\infty^\mu + \frac{\varepsilon_0^\mu - \varepsilon_\infty^\mu}{(\omega_{TO}^\mu)^2 - \omega^2 - i\gamma^\mu\omega}(\omega_{TO}^\mu)^2 \quad \text{with} \quad \mu = x, z, \text{or } SiO_2. \tag{6}$$

Here, ω_{TO}^μ is the transverse optical phonon frequency, γ^μ is a damping constant, and ε_∞^μ and ε_0^μ are the values of $\varepsilon_\mu(\omega)$ for $\omega \gg \omega_{TO}^\mu$, and $\omega \ll \omega_{TO}^\mu$, respectively. The longitudinal optical frequency ω_{LO}^μ is the frequency for which $\varepsilon_\mu(\omega) = 0$ and is given in terms of ω_{TO}^μ by the Lyddane-Sachs-Teller relation[12]: $\omega_{LO}^\mu = \omega_{TO}^\mu(\varepsilon_0^\mu/\varepsilon_\infty^\mu)^{1/2}$. The real and imaginary parts of the dielectric functions of hBN and SiO_2 are shown in Fig. SI- 10.

The influence of the graphene mono-layer is entailed through the inclusion of its sheet conductivity σ. For low energies ($\hbar\omega \ll E_F$, where E_F is the *Fermi energy*), the sheet conductivity of graphene is given by the *Drude conductivity*, σ_D as follows[13]

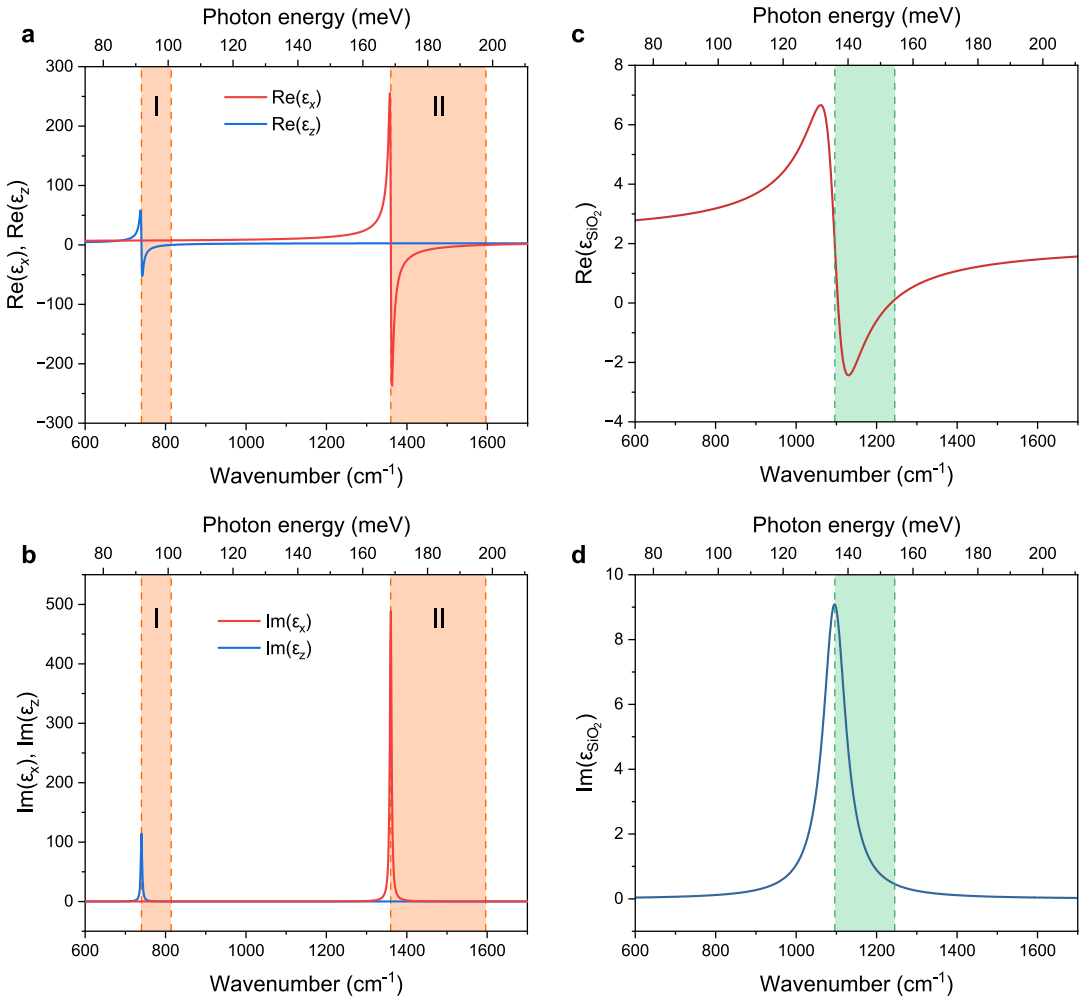

Fig. SI- 10: **a** & **b**, Real and imaginary parts of the dielectric function of hBN, obtained by applying Eq. (6) for the in-plane (x and y) and out-of-plane (z) directions. The orange-shaded regions indicate the two *Reststrahlen* bands of hBN. The optical constants appropriate for hBN are $\varepsilon_\infty^z = 2.95$, $\varepsilon_0^z = 3.57$, $\omega_{\rm TO}^z = 740$ cm^{-1}, $\omega_{\rm LO}^z = 814$ cm^{-1}, and $\gamma^z = 4$ cm^{-1}, for the out-of-plane direction (type I *Reststrahlen* band), and $\varepsilon_\infty^x = 4.87$, $\varepsilon_0^x = 6.71$, $\omega_{\rm TO}^x = 1360$ cm^{-1}, $\omega_{\rm LO}^x = 1596.4$ cm^{-1}, and $\gamma^x = 5$ cm^{-1} for the in-plane direction (type II *Reststrahlen* band). **c** & **d**, Real and imaginary parts of the dielectric function of SiO_2. The green-shaded region indicates the *Reststrahlen* band of SiO_2. Optical constants: $\varepsilon_\infty^{\rm SiO_2} = 1.97$, and $\varepsilon_0^{\rm SiO_2} = 2.54$, $\omega_{\rm TO}^{\rm SiO_2} = 1096$ cm^{-1}, $\omega_{\rm LO}^{\rm SiO_2} = 1245$ cm^{-1}, and $\gamma^{\rm SiO_2}$.

$$\sigma(\omega) = \sigma_D(\omega) = \frac{E_F e^2}{\pi\hbar}\frac{i}{\hbar(\omega + i\Gamma)}. \tag{7}$$

In the above relation, $\Gamma = ev_F^2/\mu_e E_F$, represents the phenomenological scattering rate or damping constant of electrons due to impurity scattering, in which μ_e is the electron mobility, and $v_F \approx 10^6$ m/s is the Fermi velocity.
In general, the sheet conductivity of graphene can be cast in the following form[9,14]

$$\sigma(k_x,\omega) = -\frac{ie^2}{4\hbar}\frac{\xi}{\sqrt{v_F^2k_x^2 - \xi^2}}\left[1 + G\left(\frac{\hbar\xi + 2E_F}{\hbar v_F k_x}\right) - G\left(\frac{\hbar\xi - 2E_F}{\hbar v_F k_x}\right)\right] - \frac{2i}{\pi}\frac{e^2\omega E_F}{(\hbar v_F k_x)^2}, \tag{8}$$

where, $G(\eta) = -\frac{1}{\pi}\left(\eta\sqrt{1-\eta^2} - \cos^{-1}(\eta)\right)$, $\xi = \omega + i\frac{\Gamma}{\hbar}$, and k_x is the in-plane polariton wavevector.

Assuming that the thicknesses of the encapsulating hBN layers are d_1 and d_2 (see Fig. SI- 9), we may divide the hBN/graphene/hBN/SiO_2 heterostructure of Fig. SI- 9 into the following four regions: $z > 0$ ($j = 0$, vacuum), $-d_1 < z < 0$ ($j = 1$, hBN), $-d_1 - d_2 < z < -d_1$ ($j = 2$, hBN), and $z < -d_1 - d_2$ ($j = 3$, SiO_2). The total reflection

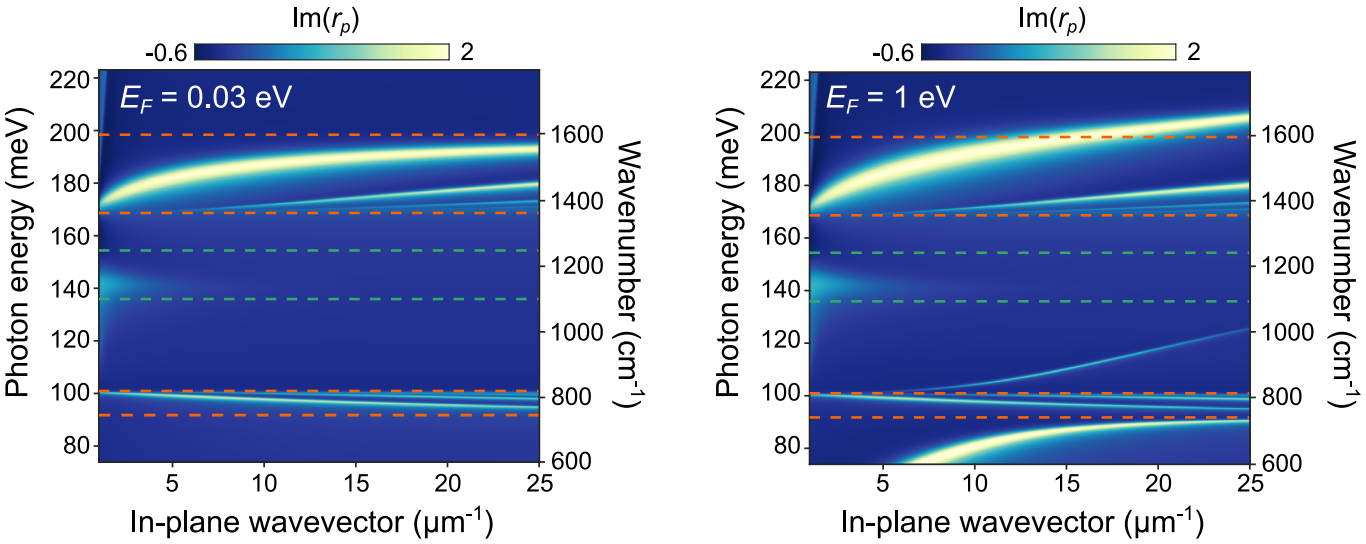

Fig. SI- 11: HPhP-plasmon dispersion curves visualized through the maxima of the imaginary part of the reflection coefficient r_p, for two different values of the Fermi energy ($E_F = 30$ meV, left; $E_F = 1$ eV, right) and electron mobility $\mu_e = 66,000$ cm^2/V.s. The thicknesses of the hBN layers are given by: $d_1 = 52$ nm and $d_2 = 30$ nm. The dashed orange and green lines enclose the *Reststrahlen* bands of hBN and SiO_2, respectively.

coefficient of the structure can then be obtained by adding the two hBN thin films successively as follows. The reflection coefficient for the first film is written as

$$r'_p = \frac{r_{12} + r_{23}(1 - r_{12} - r_{21})e^{2ik_z d_2}}{1 - r_{21} r_{23} e^{2ik_z d_2}}. \tag{9}$$

The addition of the second film yields the total reflection coefficient of the stack:

$$r_p = \frac{r_{01} + r'_p(1 - r_{01} - r_{10})e^{2ik_z d_1}}{1 - r_{10} r^1_p e^{2ik_z d_1}}. \tag{10}$$

In the above two equations, $r_{12} = (Q_2 - Q_1 + S)/(Q_1 + Q_2 + S)$ and $r_{21} = (Q_1 - Q_2 + S)/(Q_1 + Q_2 + S)$ are the reflection coefficients at the graphene/hBN boundaries, $r_{mn} = -r_{nm} = (Q_n - Q_m)/(Q_n + Q_m)$ $(mn \neq 12, 21)$ the reflection coefficients at the boundary between regions m and n, in which the following definitions were used

$$k_z = \sqrt{\varepsilon_x \left(\frac{\omega^2}{c^2} - \frac{k_x^2}{\varepsilon_z}\right)}, \quad k_{z0,3} = \sqrt{\varepsilon_{0,3}\frac{\omega^2}{c^2} - k_x^2}, \quad \mathrm{Im}(k_z, k_{z0,3}) > 0, \quad Q_{1,2} = \frac{\varepsilon_x}{k_z}, \quad Q_{0,3} = \frac{\varepsilon_{0,3}}{k_{z0,3}},$$
$$\varepsilon_0 = 1, \quad \varepsilon_3 = \varepsilon_{SiO_2}, \quad \text{and} \quad S = \frac{1}{\epsilon_\circ}\frac{\sigma(k_x, \omega)}{\omega}. \tag{11}$$

In the definitions above, $\epsilon_\circ$ is the permittivity of free space, and k_z and $k_{z0,3}$ give the out-of-plane polariton wavevector for $j = 1, 2$ and $j = 0, 3$, respectively.

The polariton branches, visualized from the maxima of the imaginary part of the reflection coefficient r_p (Eq. (10)), are shown in Fig. SI- 11 for two different values of the Fermi energy (0.03 eV and 1 eV). As presented in Fig. SI- 11, the influence of graphene's plasmons on the HPhP branches of hBN becomes important only for high Fermi energies ($E_F = 1$ eV) and is almost completely negligible when the graphene is close to neutrality (see Fig. SI- 11, $E_F = 0.03$ eV).

VI Noise thermometry comparison of the three hBN crystals

Following the approach described in Refs.[15,16] we perform noise thermometry characterization of hBN-encapsulated graphene transistors under large bias, to compare the efficiency of near-field radiative energy transfer associated with

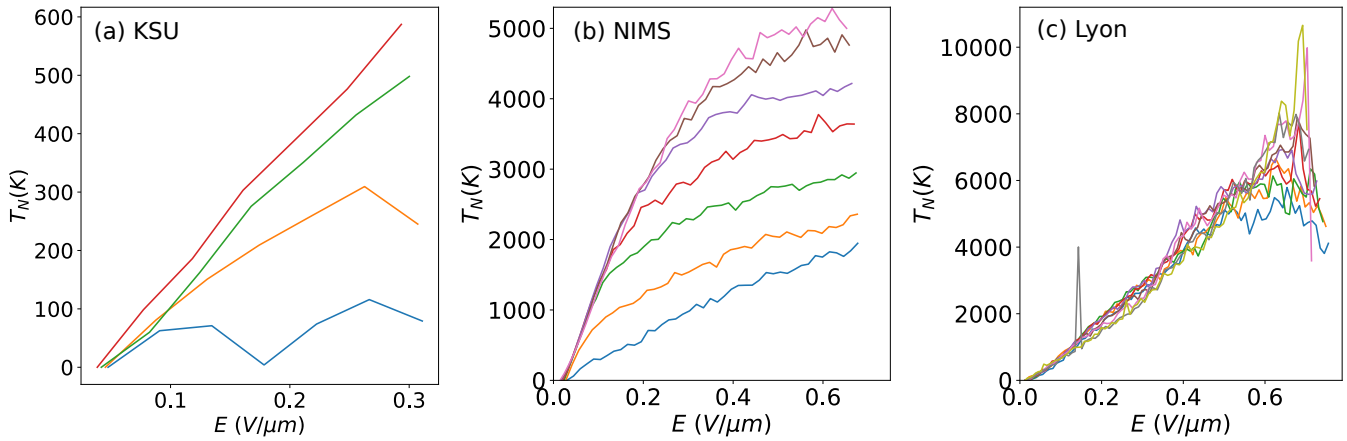

Fig. SI- 12: Electronic noise temperature as a function of bias for devices made with different hexagonal boron nitrides synthesized with various techniques, for the same doping range $n = [0-1]\ 10^{12}$ cm^{-2}. (a) Electronic noise temperature of a device made with mono-isotopic boron nitride from KSU (>99% ^{11}B, fabricated at high temperature and atmospheric pressure). (b) Electronic noise temperature of a device made with HPHT-hBN from NIMS, Japan. (c) Electronic noise temperature of a device made with PDC-hBN from Lyon, France. Strikingly, the measured noise temperature in the KSU device is much lower than previously observed. Compared with devices made with HPHT-hBN from NIMS and PDC-hBN from Lyon, the noise temperature is lower by a factor of ~ 10.

the three different hBN crystals: HPHT-hBN from NIMS, PDC-hBN from Lyon and boron-11 mono-isotopic h^{11}BN from KSU. Fig. SI- 12 shows the noise temperature curves for three representative devices and confirms (i) that radiative energy transfer is reduced in PDC-hBN and (ii) radiative energy transfer is enhanced with mono-isotopic hBN, with a much smaller noise temperature.

---

* These two authors contributed equally to this work.

[1] A Schmitt, L Abou-Hamdan, M Tharrault, S Rossetti, D Mele, R Bretel, A Pierret, M Rosticher, P Morfin, T Taniguchi, et al. Electroluminescence of the graphene 2d semi-metal. *arXiv preprint arXiv:2306.05351*, 2023.

[2] C Li, V Krachmalnicoff, P Bouchon, J Jaeck, N Bardou, R Haïdar, and Y De Wilde. Near-field and far-field thermal emission of an individual patch nanoantenna. *Phys. Rev. Lett.*, 121(24):243901, 2018.

[3] L Abou-Hamdan, C Li, R Haidar, V Krachmalnicoff, P Bouchon, and Y De Wilde. Hybrid modes in a single thermally excited asymmetric dimer antenna. *Opt. Lett.*, 46(5):981–984, 2021.

[4] L Abou-Hamdan, L Coudrat, S Bidault, V Krachmalnicoff, R Haïdar, P Bouchon, and Y De Wilde. Transition from phononic to geometrical mie modes measured in single subwavelength polar dielectric spheres. *ACS Photonics*, 9(7):2295–2303, 2022.

[5] E Pop. Energy dissipation and transport in nanoscale devices. *Nano Res.*, 3(3):147–169, 2010.

[6] E Mercado, C Yuan, Y Zhou, J Li, JH Edgar, and M Kuball. Isotopically enhanced thermal conductivity in few-layer hexagonal Boron Nitride: Implications for thermal management. *ACS Appl. Nano Mater.*, 3(12):12148–12156, 2020.

[7] GR Jaffe, KJ Smith, K Watanabe, T Taniguchi, MG Lagally, MA Eriksson, and VW Brar. Thickness-dependent cross-plane thermal conductivity measurements of exfoliated hexagonal Boron Nitride. *ACS Appl. Mater. Interfaces*, 15(9):12545–12550, 2023.

[8] S Dai, Z Fei, Q Ma, AS Rodin, M Wagner, AS McLeod, MK Liu, W Gannett, W Regan, K Watanabe, et al. Tunable phonon polaritons in atomically thin van der waals crystals of boron nitride. *Science*, 343(6175):1125–1129, 2014.

[9] S Dai, Q Ma, MK Liu, T Andersen, Z Fei, MD Goldflam, M Wagner, K Watanabe, T Taniguchi, M Thiemens, et al. Graphene on hexagonal boron nitride as a tunable hyperbolic metamaterial. *Nat. Nanotechnol.*, 10(8):682–686, 2015.

[10] KL Kliewer and R Fuchs. *Theory of dynamical properties of dielectric surfaces*, volume 27. Wiley, UK, 1974.

[11] VM Agranovich. *Surface polaritons*. Elsevier, 2012.

[12] RH Lyddane, RG Sachs, and E Teller. On the polar vibrations of alkali halides. *Phys. Rev.*, 59(8):673, 1941.

[13] MS Ukhtary and R Saito. Surface plasmons in graphene and carbon nanotubes. *Carbon*, 167:455–474, 2020.

[14] B Wunsch, T Stauber, F Sols, and F Guinea. Dynamical polarization of graphene at finite doping. *New J. Phys.*, 8(12):318, 2006.

[15] W Yang, S Berthou, X Lu, Q Wilmart, A Denis, M Rosticher, T Taniguchi, K Watanabe, G Fève, JM Berroir, et al. A graphene zener–klein transistor cooled by a hyperbolic substrate. *Nat. Nanotechnol.*, 13(1):47–52, 2018.

[16] A Schmitt, D Mele, M Rosticher, T Taniguchi, K Watanabe, C Maestre, C Journet, V Garnier, G Fève, JM Berroir, et al. High-field 1/f noise in hbn-encapsulated graphene transistors. *Phys. Rev. B*, 107(16):L161104, 2023.